Communications on Applied Mathematics and Computation (2023) 5:64–96
https://doi.org/10.1007/s42967-021-00122-9

ORIGINAL PAPER

New Finite Difference Mapped WENO Schemes with Increasingly High Order of Accuracy

Jun Zhu[1] · **Jianxian Qiu**[2]

Received: 25 October 2020 / Revised: 25 January 2021 / Accepted: 28 January 2021 /
Published online: 23 June 2021

Abstract
In this paper, a new type of finite difference mapped weighted essentially non-oscillatory (MWENO) schemes with unequal-sized stencils, such as the seventh-order and ninth-order versions, is constructed for solving hyperbolic conservation laws. For the purpose of designing increasingly high-order finite difference WENO schemes, the equal-sized stencils are becoming more and more wider. The more we use wider candidate stencils, the bigger the probability of discontinuities lies in all stencils. Therefore, one innovation of these new WENO schemes is to introduce a new splitting stencil methodology to divide some four-point or five-point stencils into several smaller three-point stencils. By the usage of this new methodology in high-order spatial reconstruction procedure, we get different degree polynomials defined on these unequal-sized stencils, and calculate the linear weights, smoothness indicators, and nonlinear weights as specified in Jiang and Shu (J. Comput. Phys. 126: 202228, 1996). Since the difference between the nonlinear weights and the linear weights is too big to keep the optimal order of accuracy in smooth regions, another crucial innovation is to present the new mapping functions which are used to obtain the mapped nonlinear weights and decrease the difference quantity between the mapped nonlinear weights and the linear weights, so as to keep the optimal order of accuracy in smooth regions. These new MWENO schemes can also be applied to compute some extreme examples, such as the double rarefaction wave problem, the Sedov blast wave problem, and

Jun Zhu: Research was supported by the NSFC grant 11872210 and the Science Challenge Project, No. TZ2016002. The author was also partly supported by the NSFC Grant 11926103 when he visited Tianyuan Mathematical Center in Southeast China, Xiamen 361005, Fujian, China.
Jianxian Qiu: Research was supported by the NSFC Grant 12071392 and the Science Challenge Project, No. TZ2016002.

✉ Jianxian Qiu
jxqiu@xmu.edu.cn

Jun Zhu
zhujun@nuaa.edu.cn

[1] College of Science, Nanjing University of Aeronautics and Astronautics, Nanjing 210016, Jiangsu, China

[2] School of Mathematical Sciences and Fujian Provincial Key Laboratory of Mathematical Modeling and High-Performance Scientific Computing, Xiamen University, Xiamen 361005, Fujian, China

the Leblanc problem with a normal CFL number. Extensive numerical results are provided to illustrate the good performance of the new finite difference MWENO schemes.

Keywords Finite difference · Mapped WENO scheme · Mapping function · Mapped nonlinear weight · Unequal-sized stencil · Extreme example

Mathematics Subject Classification 65M60 · 35L65

1 Introduction

In this paper, we propose the new seventh-order and ninth-order finite difference mapped weighted essentially non-oscillatory (MWENO) schemes with unequal-sized stencils for solving the hyperbolic conservation laws on structured meshes. Let us start by mentioning a few features and advantages of the new high-order finite difference MWENO schemes. The first is that a new splitting stencil methodology is designed to divide some four-point or five-point stencils into several smaller three-point stencils in the spatial reconstruction procedure, for the purpose of avoiding the strong discontinuities lie in all candidate wider equal-sized stencils. These unequal-sized stencils are very different from the equal-sized stencils adopted in the spatial reconstructions of the classical high-order finite difference WENO schemes [3] (which introduced the construction of monotonicity preserving interpolation strategies [29, 47] and had a smaller CFL number [3]). The second is that a series of new mapping functions are proposed by obeying the similar principles proposed by Henrick et al. [20]. Such new mapping functions are applied to decrease the difference quantity of the mapped nonlinear weight and the linear weight from $O(\Delta x^r)$ to $O(\Delta x^{3r})$–$O(\Delta x^{11r})$, so as to obtain high-order accuracy in smooth regions and have sharp non-oscillatory transitions nearby the shock waves or contact discontinuities. The third is that the largest spatial stencil of the new MWENO schemes is no bigger than that of the classical same-order finite difference WENO schemes [3, 24, 44], and these new MWENO schemes could get smaller truncation errors in L^1 and L^∞ norms and obtain the designed order of accuracy in smooth regions. The last is that these new MWENO schemes can be applied to compute rather extreme examples, such as the double rarefaction wave problem, the Sedov blast wave problem, and the Leblanc problem with a normal CFL number and without introducing any positivity preserving procedures [53–56].

Numerical solutions to the compressible Euler equations have smooth structures interspersed with strong discontinuities in the computational field. Therefore, the big challenge is to develop numerical schemes that are highly accurate in smooth regions and keep non-oscillatory property in non-smooth regions. Thereafter, Colella and Woodward [10] designed a piecewise parabolic method (PPM), which employs a four-point centered stencil to define the interface value and the value is limited to control spurious oscillations. Later, Leonard [28] combined the limiting procedure with the application of a high-order interface value. However, these limiting procedures degenerate the high-order numerical accuracy to first order even near smooth extrema. And it is well known that the PPM is an extension of the MUSCL scheme [48] and the MUSCL scheme is an extension of the Godunov's scheme [15]. For the purpose of achieving high order of accuracy, Harten and Osher [19] proposed a weaker version of the TVD measurement [16] and gave a new basis for the formulation of high-order essentially non-oscillatory (ENO) schemes. After that, Harten et al. [18] fulfilled the application of these ENO schemes in simulating one-dimensional problems. The most crucial spirit of these

ENO schemes is to use the nodal information of the smoothest stencil among all acceptable stencils for approaching the variables at the half points or cell interfaces to obtain a high-order accuracy and escape unnecessary oscillations nearby strong shocks or contact discontinuities. In 1987, Harten first proposed a two-dimensional extension of the finite volume ENO scheme in [17]. Then, Casper [7] and Casper and Atkins [8] studied the finite volume approach in developing multi-dimensional high-order accurate ENO schemes for solving the hyperbolic conservation laws. The finite difference ENO schemes were presented in [45, 46]. In 1994, Liu et al. [33] came up with a first weighted ENO scheme in a finite volume version that formatted from an rth-order ENO scheme to obtain an $(r+1)$th-order accuracy in smooth regions. In 1996, Jiang and Shu [24] further improved the above-mentioned WENO scheme [33] and approached a $(2r-1)$th-order accuracy in a finite difference version. In 1999, Hu and Shu [23] presented third-order and fourth-order finite volume WENO schemes on triangular meshes. In 2009, Zhang and Shu [52] constructed a third-order WENO scheme on tetrahedral meshes. And the optimized WENO schemes [49], monotonicity preserving WENO schemes [3], hybrid compact WENO schemes [35, 41], robust WENO schemes [22, 34, 42], and central/compact WENO (CWENO) schemes [1, 6, 11, 13, 25, 30, 31, 38] were also developed with various advantages. For solving compressible gas dynamics problems, the WENO schemes with high-order accuracy [36] are based on local characteristic decompositions and numerical flux splitting methods for the sake of suppressing spurious oscillations near discontinuities. These classical finite difference and finite volume WENO schemes [7, 8, 17, 23, 24, 33, 43, 45, 46, 51, 52] have been quite successful in numerical simulations, especially for some problems containing strong shocks, contact discontinuities, and complex small structures.

In 2005, Henrick et al. [20] found that the fifth-order WENO [24] has only third-order accuracy at the critical points in smooth regions. Therefore, they adopted a simple mapping function to the original weights in [24] and designed a mapped WENO method to achieve the fifth-order accuracy near critical points in smooth regions. Later, Feng et al. [12] studied the mapped WENO scheme [20] and found a fact that the mapping function specified in [20] may amplify the effect from the non-smooth stencils and cause a potential loss of accuracy near strong discontinuities. Bryson and Levy gave mapped WENO and weighted power ENO reconstructions in semi-discrete central schemes [5] for the Hamilton-Jacobi equations. They studied such high-order schemes by combining the Kurganov-Noelle-Petrova flux with the weighted power ENO [39, 40] and the mapped WENO reconstructions [20]. In [20], the mapped WENO interpolations improved the accuracy of the WENO reconstructions using a nonlinear mapping of the WENO weights. And they also conducted a study on the effect of composing the mapped WENO reconstruction on top of the weighted power ENO interpolations for the first time. In 2013, Gao and Don applied a mapped hybrid central-WENO scheme [14] for calculating detonation waves. More recently, Hong et al. proposed a mapping-function-free WENO-M scheme with low computational cost in [21]. Generally speaking, since the classical WENO scheme [24] lost its accuracy at the critical points in smooth regions, an extra mapping function was introduced by Henrick and other researchers [5, 12, 14, 20, 21] to overcome this drawback with significantly increased numerical accuracy near the smooth extrema.

In this paper, we present a new type of high-order finite difference MWENO schemes with unequal-sized stencils. For simplicity, we only design the seventh-order and ninth-order MWENO schemes as examples. For the purpose of constructing high-order finite difference WENO schemes with the equal-sized stencils, the wider stencils are applied and the information of the nodal points defined on them is used to reconstruct

high-degree polynomials to approximate variables at the half points. It is hard to directly apply high-order WENO schemes [3] (beyond fifth-order accuracy) with bigger CFL numbers for solving some extreme examples, such as the interaction of the blast wave problem [24] which has very large/small pressure, the one-dimensional and two-dimensional Sedov blast wave problems [26, 37] which have very low density and strong shocks, and the Leblanc problem [32] which has large pressure and small density, since the four-point or five-point stencils are too wide and the discontinuities might lie in all candidate equal-sized stencils and thus result in the appearance of the oscillations. The more we use wider candidate stencils, the bigger the probability of discontinuities lies in all stencils. An acceptable remedy is to divide some four-point or five-point stencils into several smaller three-point stencils, so as to decrease the probability of the discontinuities lying in all stencils. However, one major difficulty of such splitting stencil methodology is its wastage of high-order accuracy for the unequal degree polynomials defined on these unequal-sized stencils and the difference quantity between the nonlinear weights and the linear weights will not obey the principle proposed by Jiang and Shu in [24] any more, leading to the loss of accuracy in smooth regions. We should define a series of new mapping functions to obtain the mapped nonlinear weights to decrease associated difference quantity between the mapped nonlinear weights and the linear weights to a satisfactory quantity for the sake of sustaining the designed high-order accuracy in smooth regions. We should emphasize a fact that the usage of the new mapping functions is very different from [4, 5, 9, 12, 14, 20, 21] and our purpose of applying such new mapping functions is not to specifically increase numerical accuracy at the smooth extrema, but to gain the optimal order of accuracy in general smooth regions.

The organization of the paper is as follows. In Sect. 2, we review the new seventh-order and ninth-order finite difference MWENO schemes with unequal-sized stencils including the computation of the linear weights, smoothness indicators, and nonlinear weights. We also analyze the truncation error of the smoothness indicators, and construct five different new mapping functions to obtain the mapped nonlinear weights and decrease the difference quantity of the mapped nonlinear weights and the linear weights from $O(h^r)$ to $O(h^{3r})$ –$O(h^{11r})$. In Sect. 3, some benchmark numerical examples including low density (vacuum) and low pressure with strong shocks are presented to verify the numerical accuracy, efficiency, and robustness of the new high-order finite difference MWENO schemes. Concluding remarks are given in Sect. 4.

2 High-Order Finite Difference MWENO Schemes

In this section, we first design the new seventh-order and ninth-order finite difference mapped WENO schemes for solving the one-dimensional hyperbolic conservation laws:

$$\begin{cases} u_t + f_x(u) = 0, \\ u(x,0) = u_0(x). \end{cases} \tag{1}$$

The semi-discretization formula is written as

$$\frac{\mathrm{d}u}{\mathrm{d}t} = L(u), \tag{2}$$

where $L(u)$ is the high-order spatial discretization formulation of $-f_x(u)$. For simplicity, the mesh is uniformly distributed into cells $I_i = [x_{i-1/2}, x_{i+1/2}]$, with the cell size

$x_{i+1/2} - x_{i-1/2} = h$ and cell centers $x_i = \frac{1}{2}(x_{i+1/2} + x_{i-1/2})$, and $u_i(t)$ is defined as the approximation to $u(x_i, t)$. Herein, the right-hand side of (2) can be written as

$$L(u_i(t)) = -\frac{1}{h}(\hat{f}_{i+1/2} - \hat{f}_{i-1/2}), \tag{3}$$

where $\hat{f}_{i+1/2}$ is a numerical flux which is a high-order approximation to function v at the boundary $x_{i+1/2}$ of target cell I_i, where v is an implicit function defined as $f(u) = \frac{1}{h}\int_{x_{i-1/2}}^{x_{i+1/2}} v(\xi)\mathrm{d}\xi$. If the numerical flux $\hat{f}_{i+1/2}$ is taken to be the $(2r+1)$th-order approximation to v at $x_{i+1/2}$, then $\frac{1}{h}(\hat{f}_{i+1/2} - \hat{f}_{i-1/2})$ is the $(2r+1)$th-order approximation to $f_x(u)$ at $x = x_i$. For an ordinary flux $f(u)$, it can be split into two parts: $f(u) = f^+(u) + f^-(u)$ with $\frac{\mathrm{d}f^+(u)}{\mathrm{d}u} \geqslant 0$ and $\frac{\mathrm{d}f^-(u)}{\mathrm{d}u} \leqslant 0$. Here, a simplest Lax-Friedrichs splitting is applied

$$f^{\pm}(u) = \frac{1}{2}(f(u) \pm \alpha u), \tag{4}$$

in which α is defined as $\alpha = \max_u |f'(u)|$ over the whole range of u. Let $\hat{f}^+_{i+1/2}$ and $\hat{f}^-_{i+1/2}$ be the numerical fluxes at $x_{i+1/2}$ for the positive and negative parts of $f(u)$, respectively, and $\hat{f}_{i+1/2}$ is defined as $\hat{f}^+_{i+1/2} + \hat{f}^-_{i+1/2}$.

Now, we only describe the reconstruction procedure of $\hat{f}^+_{i+1/2}$, since the reconstruction procedure of $\hat{f}^-_{i+1/2}$ is mirror symmetric with respect to $x_{i+1/2}$ of that for $\hat{f}^+_{i+1/2}$.

Step (i) Choose the big stencil $T = \{I_{i-r}, \cdots, I_{i+r}\}$ and construct the $2r$ degree polynomial $p(x)$ satisfying

$$\frac{1}{h}\int_{I_j} p(x)\mathrm{d}x = f_j^+ = f^+(u_j),\ j = i-r, \cdots, i+r. \tag{5}$$

The values of the function $p(x)$ at the half point $x_{i+1/2}$ can be written as a linear combination of $\{f_j^+\}$. For example, if $r = 3$, we get

$$p(x_{i+1/2}) = \frac{-3f^+_{i-3} + 25f^+_{i-2} - 101f^+_{i-1} + 319f^+_i + 214f^+_{i+1} - 38f^+_{i+2} + 4f^+_{i+3}}{420}. \tag{6}$$

And if $r = 4$, we get

$$\begin{aligned} p(x_{i+1/2}) =& (4f^+_{i-4} - 41f^+_{i-3} + 199f^+_{i-2} - 641f^+_{i-1} + 1\,879f^+_i + 1\,375f^+_{i+1} - 305f^+_{i+2} + \\ & 55f^+_{i+3} - 5f^+_{i+4})/2\,520. \end{aligned} \tag{7}$$

Step (ii) Then, a modified classical WENO procedure with unequal-sized stencils is fulfilled in the following. The big stencil T is divided into some unequal-sized smaller stencils. For the seventh-order scheme, we have $r = 3$ and the smaller unequal-sized stencils are $S_1 = \{I_{i-3}, I_{i-2}, I_{i-1}, I_i\}$, $S_2 = \{I_{i-2}, I_{i-1}, I_i\}$, $S_3 = \{I_{i-1}, I_i, I_{i+1}\}$, $S_4 = \{I_i, I_{i+1}, I_{i+2}\}$, and $S_5 = \{I_i, I_{i+1}, I_{i+2}, I_{i+3}\}$. We construct different degree polynomials $p_n(x)$ on these stencils, such that

$$\begin{aligned} \frac{1}{h}\int_{I_{i-l}} p_1(x)\mathrm{d}x =& f^+_{i-l}, \quad l = 0, 1, 2, 3, \\ \frac{1}{h}\int_{I_{i-4+n+l}} p_n(x)\mathrm{d}x =& f^+_{i-4+n+l}, \quad n = 2, 3, 4; l = 0, 1, 2, \end{aligned}$$

and

$$\frac{1}{h}\int_{I_{i+l}} p_5(x)\mathrm{d}x = f^+_{i+l}, \quad l = 0, 1, 2, 3.$$

The values of reconstructed polynomials $p_n(x)$, $n = 1, \cdots, 5$ at the half point $x_{i+/2}$ are a linear combination of $\{f^+_j\}$:

$$p_1(x_{i+1/2}) = (-3f^+_{i-3} + 13f^+_{i-2} - 23f^+_{i-1} + 25f^+_i)/12, \tag{8}$$

$$p_2(x_{i+1/2}) = (2f^+_{i-2} - 7f^+_{i-1} + 11f^+_i)/6, \tag{9}$$

$$p_3(x_{i+1/2}) = (-f^+_{i-1} + 5f^+_i + 2f^+_{i+1})/6, \tag{10}$$

$$p_4(x_{i+1/2}) = (2f^+_i + 5f^+_{i+1} - f^+_{i+2})/6, \tag{11}$$

$$p_5(x_{i+1/2}) = (3f^+_i + 13f^+_{i+1} - 5f^+_{i+2} + f^+_{i+3})/12. \tag{12}$$

For the ninth-order scheme, we have $r = 4$ and the smaller unequal-sized stencils are $S_1 = \{I_{i-4}, I_{i-3}, I_{i-2}, I_{i-1}, I_i\}$,$S_2 = \{I_{i-3}, I_{i-2}, I_{i-1}, I_i, I_{i+1}\}$,$S_3 = \{I_{i-2}, I_{i-1}, I_i\}$,$S_4 = \{I_{i-1}, I_i, I_{i+1}\}$, $S_5 = \{I_i, I_{i+1}, I_{i+2}\}$, $S_6 = \{I_{i-1}, I_i, I_{i+1}, I_{i+2}, I_{i+3}\}$, and $S_7 = \{I_i, I_{i+1}, I_{i+2}, I_{i+3}, I_{i+4}\}$. We construct different degree polynomials $p_n(x)$ on these stencils, such that

$$\begin{aligned}
\frac{1}{h}\int_{I_{i-5+n+l}} p_n(x)\mathrm{d}x &= f^+_{i-5+n+l}, \quad n = 1, 2; l = 0, \cdots, 4,\\
\frac{1}{h}\int_{I_{i-5+n+l}} p_n(x)\mathrm{d}x &= f^+_{i-5+n+l}, \quad n = 3, 4, 5; l = 0, 1, 2,\\
\frac{1}{h}\int_{I_{i-7+n+l}} p_n(x)\mathrm{d}x &= f^+_{i-7+n+l}, \quad n = 6, 7;\ l = 0, \cdots, 4.
\end{aligned}$$

The values of reconstructed polynomials $p_n(x)$, $n = 1, \cdots, 7$ at the half point $x_{i+1/2}$ are a linear combination of $\{f^+_j\}$:

$$p_1(x_{i+1/2}) = (12f^+_{i-4} - 63f^+_{i-3} + 137f^+_{i-2} - 163f^+_{i-1} + 137f^+_i)/60, \tag{13}$$

$$p_2(x_{i+1/2}) = (-3f^+_{i-3} + 17f^+_{i-2} - 43f^+_{i-1} + 77f^+_i + 12f^+_{i+1})/60, \tag{14}$$

$$p_3(x_{i+1/2}) = (2f^+_{i-2} - 7f^+_{i-1} + 11f^+_i)/6, \tag{15}$$

$$p_4(x_{i+1/2}) = (-f^+_{i-1} + 5f^+_i + 2f^+_{i+1})/6, \tag{16}$$

$$p_5(x_{i+1/2}) = (2f^+_i + 5f^+_{i+1} - f^+_{i+2})/6, \tag{17}$$

$$p_6(x_{i+1/2}) = (-3f^+_{i-1} + 27f^+_i + 47f^+_{i+1} - 13f^+_{i+2} + 2f^+_{i+3})/60, \tag{18}$$

$$p_7(x_{i+1/2}) = (12f^+_i + 77f^+_{i+1} - 43f^+_{i+2} + 17f^+_{i+3} - 3f^+_{i+4})/60. \tag{19}$$

Step (iii) Then, we compute the linear weights on condition that the following equation is valid:

$$p(x_{i+1/2}) = \sum_{n=1}^{m} \gamma_n p_n(x_{i+1/2}).$$

For example, if $r = 3$, we get

$$\gamma_1 = \frac{1}{35}, \gamma_2 = \frac{3}{35}, \gamma_3 = \frac{18}{35}, \gamma_4 = \frac{9}{35}, \gamma_5 = \frac{4}{35}. \tag{20}$$

And if $r = 4$, we get

$$\gamma_1 = \frac{1}{126}, \gamma_2 = \frac{10}{63}, \gamma_3 = \frac{1}{21}, \gamma_4 = \frac{6}{21}, \gamma_5 = \frac{3}{21}, \gamma_6 = \frac{20}{63}, \gamma_7 = \frac{5}{126}. \tag{21}$$

Step (iv) We compute the smoothness indicators β_n, which measure how smooth the functions $p_n(x)$ are in the target cell I_i. The smaller these smoothness indicators are, the smoother the functions are in the target cell. We use the same recipe for the smoothness indicators as in [2, 24]:

$$\beta_n = \sum_{\alpha=1}^{r} \int_{I_i} h^{2\alpha-1} \left(\frac{\mathrm{d}^\alpha p_n(x)}{\mathrm{d}x^\alpha} \right)^2 \mathrm{d}x. \tag{22}$$

For example, if $r = 3$, we get

$$\begin{aligned} \beta_1 =& \frac{781}{720}(-f_{i-3}^+ + 3f_{i-2}^+ - 3f_{i-1}^+ + f_i^+)^2 + \frac{13}{12}(-f_{i-3}^+ + 4f_{i-2}^+ - 5f_{i-1}^+ + 2f_i^+)^2 \\ &+ \frac{1}{36}(-2f_{i-3}^+ + 9f_{i-2}^+ - 18f_{i-1}^+ + 11f_i^+)^2, \end{aligned} \tag{23}$$

$$\beta_2 = \frac{1}{4}(f_{i-2}^+ - 4f_{i-1}^+ + 3f_i^+)^2 + \frac{13}{12}(f_{i-2}^+ - 2f_{i-1}^+ + f_i^+)^2, \tag{24}$$

$$\beta_3 = \frac{1}{4}(-f_{i-1}^+ + f_{i+1}^+)^2 + \frac{13}{12}(f_{i-1}^+ - 2f_i^+ + f_{i+1}^+)^2, \tag{25}$$

$$\beta_4 = \frac{1}{4}(-3f_i^+ + 4f_{i+1}^+ - f_{i+2}^+)^2 + \frac{13}{12}(f_i^+ - 2f_{i+1}^+ + f_{i+2}^+)^2, \tag{26}$$

$$\begin{aligned} \beta_5 =& \frac{781}{720}(-f_i^+ + 3f_{i+1}^+ - 3f_{i+2}^+ + f_{i+3}^+)^2 + \frac{13}{12}(2f_i^+ - 5f_{i+1}^+ + 4f_{i+2}^+ - f_{i+3}^+)^2 \\ &+ \frac{1}{36}(-11f_i^+ + 18f_{i+1}^+ - 9f_{i+2}^+ + 2f_{i+3}^+)^2. \end{aligned} \tag{27}$$

The expansions of (23)–(27) in Taylor series about f_i^+ are

$$\begin{aligned} \beta_1 =& (2\,160h^2((f_i^+)')^2 + 2\,340h^4((f_i^+)^{(2)})^2 - 1\,080h^5(f_i^+)'(f_i^+)^{(4)} - 7\,029h^7(f_i^+)^{(3)}(f_i^+)^{(4)} \\ &+ 7\,373h^8((f_i^+)^{(4)})^2 + 33h^6(71((f_i^+)^{(3)})^2 - 130(f_i^+)^{(2)}(f_i^+)^{(4)}))/2\,160 + O(h^9) \\ =& h^2((f_i^+)')^2(1 + O(h^3)), \end{aligned} \tag{28}$$

$$\begin{aligned}\beta_2 =&h^2((f_i^+)')^2 + h^4(13((f_i^+)^{(2)})^2 - 8(f_i^+)'(f_i^+)^{(3)})/12 - 103h^7(f_i^+)^{(3)}(f_i^+)^{(4)}/72+\\ &745h^8((f_i^+)^{(4)})^2/1\,728 - h^5(13(f_i^+)^{(2)}(f_i^+)^{(3)} - 3(f_i^+)'(f_i^+)^{(4)})/6 + h^6(86((f_i^+)^{(3)})^2\\ &+ 91(f_i^+)^{(2)}(f_i^+)^{(4)})/72 + O(h^9)\\ =&h^2((f_i^+)')^2(1 + O(h^2)),\end{aligned} \tag{29}$$

$$\begin{aligned}\beta_3 =&h^2((f_i^+)')^2 + h^4(13((f_i^+)^{(2)})^2 + 4(f_i^+)'(f_i^+)^{(3)})/12 + 13h^8((f_i^+)^{(4)})^2/1\,728 + h^6(2\\ &((f_i^+)^{(3)})^2 + 13(f_i^+)^{(2)}(f_i^+)^{(4)})/72 + O(h^9)\\ =&h^2((f_i^+)')^2(1 + O(h^2)),\end{aligned} \tag{30}$$

$$\begin{aligned}\beta_4 =&h^2((f_i^+)')^2 + h^4(13((f_i^+)^{(2)})^2 - 8(f_i^+)'(f_i^+)^{(3)})/12 + 103h^7(f_i^+)^{(3)}(f_i^+)^{(4)}/72+\\ &745h^8((f_i^+)^{(4)})^2/1\,728 + h^5(13(f_i^+)^{(2)}(f_i^+)^{(3)} - 3(f_i^+)'(f_i^+)^{(4)})/6 + h^6(86((f_i^+)^{(3)})^2\\ &+ 91(f_i^+)^{(2)}(f_i^+)^{(4)})/72 + O(h^9)\\ =&h^2((f_i^+)')^2(1 + O(h^2)),\end{aligned} \tag{31}$$

$$\begin{aligned}\beta_5 =&(2\,160h^2((f_i^+)')^2 + 2\,340h^4((f_i^+)^{(2)})^2 + 1\,080h^5(f_i^+)'(f_i^+)^{(4)} + 7\,029h^7(f_i^+)^{(3)}(f_i^+)^{(4)}\\ &+ 7\,373h^8((f_i^+)^{(4)})^2 + 33h^6(71((f_i^+)^{(3)})^2 - 130(f_i^+)^{(2)}(f_i^+)^{(4)}))/2\,160 + O(h^9)\\ =&h^2((f_i^+)')^2(1 + O(h^3)).\end{aligned} \tag{32}$$

It is assumed that the smoothness indicators can be rewritten as $\beta_1 = D(1 + O(h^3))$, $\beta_{2,3,4} = D(1 + O(h^2))$, and $\beta_5 = D(1 + O(h^3))$ on condition that $D = h^2((f_i^+)')^2$ is a non-zero constant independent of n.

If $r = 4$, we get

$$\begin{aligned}\beta_1 =&\frac{1\,421\,461}{1\,310\,400}(f_{i-4}^+ - 4f_{i-3}^+ + 6f_{i-2}^+ - 4f_{i-1}^+ + f_i^+)^2\\ &+ \frac{781}{2\,880}(3f_{i-4}^+ - 14f_{i-3}^+ + 24f_{i-2}^+ - 18f_{i-1}^+ + 5f_i^+)^2\\ &+ \frac{1}{15\,600}(119f_{i-4}^+ - 606f_{i-3}^+ + 1\,234f_{i-2}^+ - 1\,126f_{i-1}^+ + 379f_i^+)^2\\ &+ \frac{1}{1\,440}(3f_{i-4}^+ - 16f_{i-3}^+ + 36f_{i-2}^+ - 48f_{i-1}^+ + 25f_i^+)^2,\end{aligned} \tag{33}$$

$$\begin{aligned}\beta_2 =&\frac{1\,421\,461}{1\,310\,400}(f_{i-3}^+ - 4f_{i-2}^+ + 6f_{i-1}^+ - 4f_i^+ + f_{i+1}^+)^2\\ &+ \frac{781}{2\,880}(f_{i-3}^+ - 6f_{i-2}^+ + 12f_{i-1}^+ - 10f_i^+ + 3f_{i+1}^+)^2\\ &+ \frac{1}{15\,600}(-11f_{i-3}^+ + 44f_{i-2}^+ + 64f_{i-1}^+ - 216f_i^+ + 119f_{i+1}^+)^2\\ &+ \frac{1}{1\,440}(-f_{i-3}^+ + 6f_{i-2}^+ - 18f_{i-1}^+ + 10f_i^+ + 3f_{i+1}^+)^2,\end{aligned} \tag{34}$$

$$\beta_3 = \frac{1}{4}(f_{i-2}^+ - 4f_{i-1}^+ + 3f_i^+)^2 + \frac{13}{12}(f_{i-2}^+ - 2f_{i-1}^+ + f_i^+)^2, \tag{35}$$

$$\beta_4 = \frac{1}{4}(-f_{i-1}^+ + f_{i+1}^+)^2 + \frac{13}{12}(f_{i-1}^+ - 2f_i^+ + f_{i+1}^+)^2, \tag{36}$$

$$\beta_5 = \frac{1}{4}(-3f_i^+ + 4f_{i+1}^+ - f_{i+2}^+)^2 + \frac{13}{12}(f_i^+ - 2f_{i+1}^+ + f_{i+2}^+)^2, \tag{37}$$

$$\begin{aligned}\beta_6 =& \frac{1\,421\,461}{1\,310\,400}(f_{i-1}^+ - 4f_i^+ + 6f_{i+1}^+ - 4f_{i+2}^+ + f_{i+3}^+)^2 \\ &+ \frac{781}{2\,880}(-3f_{i-1}^+ + 10f_i^+ - 12f_{i+1}^+ + 6f_{i+2}^+ - f_{i+3}^+)^2 \\ &+ \frac{1}{15\,600}(119f_{i-1}^+ - 216f_i^+ + 64f_{i+1}^+ + 44f_{i+2}^+ - 11f_{i+3}^+)^2 \\ &+ \frac{1}{1\,440}(-3f_{i-1}^+ - 10f_i^+ + 18f_{i+1}^+ - 6f_{i+2}^+ + f_{i+3}^+)^2,\end{aligned} \tag{38}$$

$$\begin{aligned}\beta_7 =& \frac{1\,421\,461}{1\,310\,400}(f_i^+ - 4f_{i+1}^+ + 6f_{i+2}^+ - 4f_{i+3}^+ + f_{i+4}^+)^2 \\ &+ \frac{781}{2\,880}(-5f_i^+ + 18f_{i+1}^+ - 24f_{i+2}^+ + 14f_{i+3}^+ - 3f_{i+4}^+)^2 \\ &+ \frac{1}{15\,600}(379f_i^+ - 1\,126f_{i+1}^+ + 1\,234f_{i+2}^+ - 606f_{i+3}^+ + 119f_{i+4}^+)^2 \\ &+ \frac{1}{1\,440}(-25f_i^+ + 48f_{i+1}^+ - 36f_{i+2}^+ + 16f_{i+3}^+ - 3f_{i+4}^+)^2.\end{aligned} \tag{39}$$

The expansions of (33)–(39) in Taylor series about f_i^+ are

$$\begin{aligned}\beta_1 =& h^2((f_i^+)')^2 + 13h^4((f_i^+)^{(2)})^2/12 - 9h^7(f_i^+)^{(2)}(f_i^+)^{(5)}/5 - 21\,857h^9(f_i^+)^{(4)}(f_i^+)^{(5)}/5\,040 \\ &+ 1\,135\,501h^{10}((f_i^+)^{(5)})^2/134\,400 + h^6(781((f_i^+)^{(3)})^2 - 2(f_i^+)^{(2)}(f_i^+)^{(4)} \\ &- 288(f_i^+)'(f_i^+)^{(5)})/720 + h^8(32\,803((f_i^+)^{(4)})^2 - 114\,807(f_i^+)^{(3)}(f_i^+)^{(5)})/30\,240 + O(h^{11}) \\ =& h^2((f_i^+)')^2(1 + O(h^4)),\end{aligned} \tag{40}$$

$$\begin{aligned}\beta_2 =& h^2((f_i^+)')^2 + 13h^4((f_i^+)^{(2)})^2/12 + 11h^7(f_i^+)^{(2)}(f_i^+)^{(5)}/60 \\ &- 21\,871h^9(f_i^+)^{(4)}(f_i^+)^{(5)}/10\,080 + 156\,281h^{10}((f_i^+)^{(5)})^2/134\,400 \\ &+ h^6(781((f_i^+)^{(3)})^2 - 2(f_i^+)^{(2)}(f_i^+)^{(4)} \\ &+ 72(f_i^+)'(f_i^+)^{(5)})/720 + h^8(32\,803((f_i^+)^{(4)})^2 \\ &- 16\,401(f_i^+)^{(3)}(f_i^+)^{(5)})/30\,240 + O(h^{11}) \\ =& h^2((f_i^+)')^2(1 + O(h^4)),\end{aligned} \tag{41}$$

$$\begin{aligned}\beta_3 =&h^2((f_i^+)')^2+h^4(13((f_i^+)^{(2)})^2-8(f_i^+)'(f_i^+)^{(3)})/12-103h^7(f_i^+)^{(3)}(f_i^+)^{(4)}/72\\&+745h^8((f_i^+)^{(4)})^2/1\,728-h^5(13(f_i^+)^{(2)}(f_i^+)^{(3)}-3(f_i^+)'(f_i^+)^{(4)})/6+h^6(86((f_i^+)^{(3)})^2\\&+91(f_i^+)^{(2)}(f_i^+)^{(4)})/72+O(h^9)\\=&h^2((f_i^+)')^2(1+O(h^2)),\end{aligned}\tag{42}$$

$$\begin{aligned}\beta_4 =&h^2((f_i^+)')^2+h^4(13((f_i^+)^{(2)})^2+4(f_i^+)'(f_i^+)^{(3)})/12+13h^8((f_i^+)^{(4)})^2/1\,728\\&+h^6(2((f_i^+)^{(3)})^2+13(f_i^+)^{(2)}(f_i^+)^{(4)})/72+O(h^9)\\=&h^2((f_i^+)')^2(1+O(h^2)),\end{aligned}\tag{43}$$

$$\begin{aligned}\beta_5 =&h^2((f_i^+)')^2+h^4(13((f_i^+)^{(2)})^2-8(f_i^+)'(f_i^+)^{(3)})/12+103h^7(f_i^+)^{(3)}(f_i^+)^{(4)}/72\\&+745h^8((f_i^+)^{(4)})^2/1\,728+h^5(13(f_i^+)^{(2)}(f_i^+)^{(3)}-3(f_i^+)'(f_i^+)^{(4)})/6\\&+h^6(86((f_i^+)^{(3)})^2+91(f_i^+)^{(2)}(f_i^+)^{(4)})/72+O(h^9)\\=&h^2((f_i^+)')^2(1+O(h^2)),\end{aligned}\tag{44}$$

$$\begin{aligned}\beta_6 =&h^2((f_i^+)')^2+13h^4((f_i^+)^{(2)})^2/12-11h^7(f_i^+)^{(2)}(f_i^+)^{(5)}/60\\&+21\,871h^9(f_i^+)^{(4)}(f_i^+)^{(5)}/10\,080+156\,281h^{10}((f_i^+)^{(5)})^2/134\,400\\&+h^6(781((f_i^+)^{(3)})^2-2(f_i^+)^{(2)}(f_i^+)^{(4)}\\&+72(f_i^+)'(f_i^+)^{(5)})/720+h^8(32\,803((f_i^+)^{(4)})^2\\&-16\,401(f_i^+)^{(3)}(f_i^+)^{(5)})/30\,240+O(h^{11})\\=&h^2((f_i^+)')^2(1+O(h^4)),\end{aligned}\tag{45}$$

$$\begin{aligned}\beta_7 =&h^2((f_i^+)')^2+13h^4((f_i^+)^{(2)})^2/12+9h^7(f_i^+)^{(2)}(f_i^+)^{(5)}/5+21\,857h^9(f_i^+)^{(4)}(f_i^+)^{(5)}/5\,040\\&+1\,135\,501h^{10}((f_i^+)^{(5)})^2/134\,400+h^6(781((f_i^+)^{(3)})^2-2(f_i^+)^{(2)}(f_i^+)^{(4)}\\&-288(f_i^+)'(f_i^+)^{(5)})/720+h^8(32\,803((f_i^+)^{(4)})^2\\&-114\,807(f_i^+)^{(3)}(f_i^+)^{(5)})/30\,240+O(h^{11})\\=&h^2((f_i^+)')^2(1+O(h^4)).\end{aligned}\tag{46}$$

It is assumed that the smoothness indicators can be rewritten as $\beta_{1,2}=D(1+O(h^4))$, $\beta_{3,4,5}=D(1+O(h^2))$, and $\beta_{6,7}=D(1+O(h^4))$ on condition that $D=h^2((f_i^+)')^2$ is a nonzero constant independent of n.

Step (v) Then, the nonlinear weights based on the linear weights and the smoothness indicators [44] are

$$\omega_n^{(\mathrm{JS})}=\frac{\omega_n}{\sum_{k=1}^{m}\omega_k},\quad \omega_n=\frac{\gamma_n}{(\varepsilon+\beta_n)^2},\quad n=1,\cdots,m.\tag{47}$$

If $r=3$ and $\varepsilon\ll\beta_k$, we substitute (28)–(32) into (47) and obtain $\omega_1=\frac{\gamma_1}{D^2}(1+O(h^3))$, $\omega_2=\frac{\gamma_2}{D^2}(1+O(h^2))$, $\omega_3=\frac{\gamma_3}{D^2}(1+O(h^2))$, $\omega_4=\frac{\gamma_4}{D^2}(1+O(h^2))$, and $\omega_5=\frac{\gamma_5}{D^2}(1+O(h^3))$.

Then, we get $\omega_1 = \gamma_1 + O(h^3)$, $\omega_2 = \gamma_2 + O(h^2)$, $\omega_3 = \gamma_3 + O(h^2)$, $\omega_4 = \gamma_4 + O(h^2)$, and $\omega_5 = \gamma_5 + O(h^3)$. If $r = 4$ and $\varepsilon \ll \beta_k$, we substitute (40)–(46) into (47) and obtain $\omega_1 = \frac{\gamma_1}{D^2}(1 + O(h^4))$, $\omega_2 = \frac{\gamma_2}{D^2}(1 + O(h^4))$, $\omega_3 = \frac{\gamma_3}{D^2}(1 + O(h^2))$, $\omega_4 = \frac{\gamma_4}{D^2}(1 + O(h^2))$, $\omega_5 = \frac{\gamma_5}{D^2}(1 + O(h^2))$, $\omega_6 = \frac{\gamma_6}{D^2}(1 + O(h^4))$, and $\omega_7 = \frac{\gamma_7}{D^2}(1 + O(h^4))$. Then, we get $\omega_1 = \gamma_1 + O(h^4)$, $\omega_2 = \gamma_2 + O(h^4)$, $\omega_3 = \gamma_3 + O(h^2)$, $\omega_4 = \gamma_4 + O(h^2)$, $\omega_5 = \gamma_5 + O(h^2)$, $\omega_6 = \gamma_6 + O(h^4)$, and $\omega_7 = \gamma_7 + O(h^4)$. Herein, the associated new schemes with unequal-sized stencils could not sustain their designed order of accuracy. For the purpose of decreasing the difference quantity between the nonlinear weights and the linear weights, five different types of new mapping functions are proposed in the following.

Type (i): the mapping function is monotonically increasing with finite slope and satisfies the conditions $g_n(0) = 0$, $g_n(1) = 1$, $g_n(\gamma_n) = \gamma_n$, $g_n^{(\ell)}(\gamma_n) = 0$, $\ell = 1, 2$, and $g_n^{(3)}(\gamma_n) = \frac{3!}{(-1+\gamma_n)^2} \neq 0$,

$$g_n(\omega) = \frac{(-1+\gamma_n)^2\gamma_n\omega}{\gamma_n^3 + \omega - 2\gamma_n^2\omega - \omega^3 + \gamma_n\omega(-2+3\omega)}, \quad n = 1, \cdots, m. \tag{48}$$

If $\omega = \gamma_n + O(h^r)$, we get $g_n(\omega) = \gamma_n + O(h^{3r})$.

Type (ii): the mapping function is monotonically increasing with finite slope and satisfies the conditions $g_n(0) = 0$, $g_n(1) = 1$, $g_n(\gamma_n) = \gamma_n$, $g_n^{(\ell)}(\gamma_n) = 0$, $\ell = 1, \cdots, 4$, and $g_n^{(5)}(\gamma_n) \neq 0$,

$$\begin{aligned} g_n(\omega) =& (\omega(\gamma_n + \gamma_n^4 + \gamma_n^3(6 - 10\omega) - 5\gamma_n\omega^3 + \omega^4 + 2\gamma_n^2(-2 + 5\omega^2)))/(\gamma_n^4 + \omega \\ & - 4\gamma_n\omega + 6\gamma_n^2\omega - 4\gamma_n^3\omega), \quad n = 1, \cdots, m. \end{aligned} \tag{49}$$

If $\omega = \gamma_n + O(h^r)$, we get $g_n(\omega) = \gamma_n + O(h^{5r})$.

Type (iii): the mapping function is monotonically increasing with finite slope and satisfies the conditions $g_n(0) = 0$, $g_n(1) = 1$, $g_n(\gamma_n) = \gamma_n$, $g_n^{(\ell)}(\gamma_n) = 0$, $\ell = 1, \cdots, 6$, and $g_n^{(7)}(\gamma_n) \neq 0$,

$$\begin{aligned} g_n(\omega) =& (\omega(\gamma_n + \gamma_n^6 - 7\gamma_n\omega^5 + \omega^6 - 3\gamma_n^5(-5 + 7\omega) + 5\gamma_n^4(-4 + 7\omega^2) \\ & - 5\gamma_n^3(-3 + 7\omega^3) + 3\gamma_n^2(-2 + 7\omega^4)))/(\gamma_n^6 + \omega - 6\gamma_n\omega + 15\gamma_n^2\omega - 20\gamma_n^3\omega + 15\gamma_n^4\omega \\ & - 6\gamma_n^5\omega), \quad n = 1, \cdots, m. \end{aligned} \tag{50}$$

If $\omega = \gamma_n + O(h^r)$, we get $g_n(\omega) = \gamma_n + O(h^{7r})$.

Type (iv): the mapping function is monotonically increasing with finite slope and satisfies the conditions $g_n(0) = 0$, $g_n(1) = 1$, $g_n(\gamma_n) = \gamma_n$, $g_n^{(\ell)}(\gamma_n) = 0$, $\ell = 1, \cdots, 8$, and $g_n^{(9)}(\gamma_n) \neq 0$,

$$\begin{aligned} g_n(\omega) =& (\omega(\gamma_n + \gamma_n^8 - 9\gamma_n\omega^7 + \omega^8 - 4\gamma_n^7(-7 + 9\omega) + 28\gamma_n^6(-2 + 3\omega^2) \\ & - 14\gamma_n^5(-5 + 9\omega^3) + 14\gamma_n^4(-4 + 9\omega^4) + \gamma_n^3(28 - 84\omega^5) + 4\gamma_n^2(-2 + 9\omega^6)))/(\gamma_n^8 + \omega \\ & - 8\gamma_n\omega + 28\gamma_n^2\omega - 56\gamma_n^3\omega + 70\gamma_n^4\omega - 56\gamma_n^5\omega + 28\gamma_n^6\omega - 8\gamma_n^7\omega), \\ & n = 1, \cdots, m. \end{aligned} \tag{51}$$

If $\omega = \gamma_n + O(h^r)$, we get $g_n(\omega) = \gamma_n + O(h^{9r})$.

Type (v): the mapping function is monotonically increasing with finite slope and satisfies the conditions $g_n(0) = 0$, $g_n(1) = 1$, $g_n(\gamma_n) = \gamma_n$, $g_n^{(\ell)}(\gamma_n) = 0$, $\ell = 1, \cdots, 10$, and $g_n^{(11)}(\gamma_n) \neq 0$,

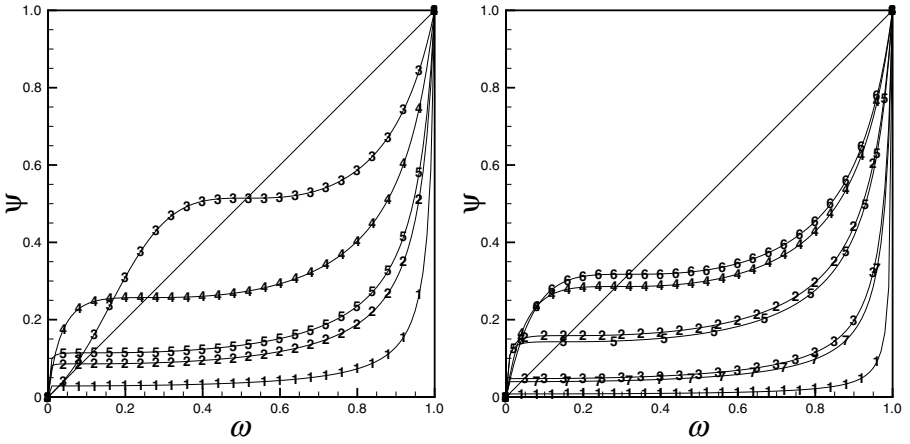

Fig. 1 Left: mapping functions with $r = 3$ and $\Psi = g_n(\omega), n = 1, \cdots, 5$. Solid line: the identity mapping; 1 and solid line: $\gamma_1 = \frac{1}{35}$; 2 and solid line: $\gamma_2 = \frac{3}{35}$; 3 and solid line: $\gamma_3 = \frac{18}{35}$; 4 and solid line: $\gamma_4 = \frac{9}{35}$; 5 and solid line: $\gamma_5 = \frac{4}{35}$. Right: mapping functions with $r = 4$ and $\Psi = g_n(\omega), n = 1, \cdots, 7$. Solid line: the identity mapping; 1 and solid line: $\gamma_1 = \frac{1}{126}$; 2 and solid line: $\gamma_2 = \frac{10}{63}$; 3 and solid line: $\gamma_3 = \frac{1}{21}$; 4 and solid line: $\gamma_4 = \frac{6}{21}$; 5 and solid line: $\gamma_5 = \frac{3}{21}$; 6 and solid line: $\gamma_6 = \frac{20}{63}$; 7 and solid line: $\gamma_7 = \frac{5}{126}$

$$
\begin{aligned}
g_n(\omega) =&(\omega(\gamma_n + \gamma_n^{10} + \gamma_n^9(45 - 55\omega) - 11\gamma_n\omega^9 + \omega^{10} + 15\gamma_n^8(-8 + 11\omega^2) \\
&- 30\gamma_n^7(-7 + 11\omega^3) + 42\gamma_n^6(-6 + 11\omega^4) - 42\gamma_n^5(-5 + 11\omega^5) + 30\gamma_n^4(-4 + 11\omega^6) \\
&+ \gamma_n^3(45 - 165\omega^7) + 5\gamma_n^2(-2 + 11\omega^8)))/(\gamma_n^{10} + \omega - 10\gamma_n\omega + 45\gamma_n^2\omega - 120\gamma_n^3\omega + 210\gamma_n^4\omega \\
&- 252\gamma_n^5\omega + 210\gamma_n^6\omega - 120\gamma_n^7\omega + 45\gamma_n^8\omega - 10\gamma_n^9\omega), \quad n = 1, \cdots, m. \qquad (52)
\end{aligned}
$$

If $\omega = \gamma_n + O(h^r)$, we get $g_n(\omega) = \gamma_n + O(h^{11r})$.

Since the type (i) mapping functions are good enough for our computations in this paper, we only show this type of mapping functions in Fig. 1 for $r = 3$ and $r = 4$ cases. And the associated Taylor series expansions of $g_n(\omega)$ for ω at γ_n yield

$$
\begin{aligned}
g_n(\omega) =& g_n(\gamma_n) + g_n'(\gamma_n)(\omega - \gamma_n) + \frac{g_n''(\gamma_n)}{2!}(\omega - \gamma_n)^2 + \frac{g_n'''(\gamma_n)}{3!}(\omega - \gamma_n)^3 \\
&+ \frac{g_n''''(\gamma_n)}{4!}(\omega - \gamma_n)^4 + \cdots = \gamma_n + \frac{(\omega - \gamma_n)^3}{(-1 + \gamma_n)^2} + \frac{(\omega - \gamma_n)^4}{(-1 + \gamma_n)^2\gamma_n} + \cdots . \qquad (53)
\end{aligned}
$$

And this mapping function satisfies the properties including: if $\omega \in [0, 1]$, then $g_n(\omega) \in [0, 1]$, $g_n(0) = 0$, and $g_n(1) = 1$; if $\omega \approx 0$, then $g_n(\omega) \approx 0$; if $\omega \approx 1$, then $g_n(\omega) \approx 1$; if $\omega = \gamma_n + O(h^r)$, then $g_n(\omega) = \gamma_n + O(h^{3r})$. Then the mapped nonlinear weights are defined as

$$
\omega_n^{(\mathrm{M})} = \frac{g_n(\omega_n^{(\mathrm{JS})})}{\sum_{k=1}^{m} g_k(\omega_k^{(\mathrm{JS})})}, \quad n = 1, \cdots, m. \qquad (54)
$$

If $r = 3$ and $\varepsilon \ll \beta_k$, we substitute (28)–(32) into (54) and obtain $\omega_1^{(\mathrm{M})} = \gamma_1 + O(h^9)$, $\omega_2^{(\mathrm{M})} = \gamma_2 + O(h^6)$, $\omega_3^{(\mathrm{M})} = \gamma_3 + O(h^6)$, $\omega_4^{(\mathrm{M})} = \gamma_4 + O(h^6)$, and $\omega_5^{(\mathrm{M})} = \gamma_5 + O(h^9)$. If $r = 4$ and $\varepsilon \ll \beta_k$, we substitute (40)–(46) into (54) and obtain $\omega_1^{(\mathrm{M})} = \gamma_1 + O(h^{12})$,

$\omega_2^{(\mathrm{M})} = \gamma_2 + O(h^{12})$, $\omega_3^{(\mathrm{M})} = \gamma_3 + O(h^6)$, $\omega_4^{(\mathrm{M})} = \gamma_4 + O(h^6)$, $\omega_5^{(\mathrm{M})} = \gamma_5 + O(h^6)$, $\omega_6^{(\mathrm{M})} = \gamma_6 + O(h^{12})$, and $\omega_7^{(\mathrm{M})} = \gamma_7 + O(h^{12})$. In our computations, we set $\varepsilon = 10^{-6}$. By doing so, the designed high order of accuracy is obtained. The final reconstruction of the numerical flux for the positive part of $f(u)$ at the half point $x = x_{i+1/2}$ is given by

$$\hat{f}^+_{i+1/2} = \sum_{n=1}^{m} \omega_n^{(\mathrm{M})} p_n(x_{i+1/2}). \tag{55}$$

Step (vi) The semi-discrete scheme (2) is discretized in time by a third-order TVD Runge-Kutta method [45]:

$$\begin{cases} u^{(1)} = u^n + \Delta t L(u^n), \\ u^{(2)} = \frac{3}{4}u^n + \frac{1}{4}u^{(1)} + \frac{1}{4}\Delta t L(u^{(1)}), \\ u^{n+1} = \frac{1}{3}u^n + \frac{2}{3}u^{(2)} + \frac{2}{3}\Delta t L(u^{(2)}). \end{cases} \tag{56}$$

Remark 1 For systems of the Euler equations, all of the reconstructions are performed in the local characteristic directions to avoid spurious oscillations. When the problems are extended to two-dimensional cases, the reconstructing procedure is executed in a dimension-by-dimension fashion.

3 Numerical Tests

In this section, we present the numerical results of some benchmark tests using the seventh-order and ninth-order MWENO schemes with unequal-sized stencils which are termed as MWENO7 and MWENO9 schemes comparing with the classical same-order WENO schemes [24, 44] which are termed as WENO7-JS and WENO9-JS schemes, respectively. These new high-order MWENO schemes can also compute some extreme examples, such as the one-dimensional and two-dimensional Sedov blast wave problems, the one-dimensional and two-dimensional double rarefaction wave problems, and the Leblanc problem with a normal CFL number and without any positivity preserving procedure [53–56] to suppress negative density and negative pressure. Therefore, the CFL number is set as 0.6 for all examples in this paper, except for the accuracy test cases, where we set $\Delta t = \frac{\mathrm{CFL}}{\alpha} h^{\frac{7}{3}}$ and $\Delta t = \frac{\mathrm{CFL}}{\alpha} h^3$ for the seventh-order and ninth-order schemes, respectively, to ensure the spatial error dominates over the temporary error.

Example 1 We solve the scalar linear equation

$$u_t + u_x = 0, \ x \in [0, 2] \tag{57}$$

with the initial condition $u(x, 0) = \sin(\pi x)$. The periodic boundary condition is applied in this test. The solution is computed up to $t = 2$. The errors and numerical orders of accuracy for the MWENO7 and MWENO9 schemes together with the WENO7-JS and WENO9-JS schemes for comparison are shown in Table 1. We can see that the new high-order

Table 1 $u_t + u_x = 0$, $u(x,0) = \sin(\pi x)$, $T = 2$, L^1 and L^∞ errors

Grid points	MWENO7 scheme				WENO7-JS scheme			
	L^1 error	Order	L^∞ error	Order	L^1 error	Order	L^∞ error	Order
10	2.25E–3		3.77E–3		3.91E–3		9.24E–3	
20	9.18E–6	7.94	1.45E–5	8.02	9.11E–5	5.42	2.42E–4	5.25
30	3.76E–7	7.88	6.43E–7	7.69	7.31E–6	6.22	2.73E–5	5.38
40	4.43E–8	7.43	7.51E–8	7.46	1.29E–6	6.00	5.79E–6	5.40
50	8.76E–9	7.26	1.44E–8	7.40	3.20E–7	6.28	1.85E–6	5.11
60	2.36E–9	7.18	3.88E–9	7.19	1.10E–7	5.81	6.91E–7	5.40
Grid points	MWENO9 scheme				WENO9-JS scheme			
	L^1 error	Order	L^∞ error	Order	L^1 error	Order	L^∞ error	Order
10	5.05E–4		9.39E–4		4.45E–4		8.31E–4	
20	5.14E–7	9.94	1.04E–6	9.81	1.14E–6	8.61	2.30E–6	8.49
30	1.09E–8	9.50	2.56E–8	9.14	2.58E–8	9.34	5.67E–8	9.13
40	7.72E–10	9.20	2.04E–9	8.79	1.83E–9	9.20	4.25E–9	9.01
50	9.95E–11	9.18	2.74E–10	9.00	2.33E–10	9.23	5.86E–10	8.87
60	1.84E–11	9.26	5.36E–11	8.96	4.43E–11	9.12	1.06E–10	9.35

MWENO schemes keep the designed order of accuracy, while the classical WENO7-JS scheme could not attain its optimal accuracy and the WENO9-JS scheme could get its optimal accuracy. And the absolute truncation errors of two classical WENO schemes are bigger than those of the associated same-order MWENO schemes. Figure 2 shows that the MWENO schemes need less CPU time than the WENO-JS schemes to obtain the same quantities of L^1 and L^∞ errors, so the MWENO schemes are more efficient than the WENO-JS schemes in this test case.

Example 2 We solve the one-dimensional Euler equations

$$\frac{\partial}{\partial t}\begin{pmatrix} \rho \\ \rho u \\ E \end{pmatrix} + \frac{\partial}{\partial x}\begin{pmatrix} \rho u \\ \rho u^2 + p \\ u(E+p) \end{pmatrix} = 0. \tag{58}$$

The initial conditions are $\rho(x,0) = 1 + 0.2\sin(\pi x)$, $u(x,0) = 1.0$, and $p(x,0) = 1$. The computing domain is $x \in [0,2]$. The periodic boundary condition is applied in this test. The exact density solution is $\rho(x,t) = 1 + 0.2\sin(\pi(x-t))$. The final time is $t = 2$. The errors and numerical orders of accuracy for the density of the MWENO7 and MWENO9 schemes together with the WENO7-JS and WENO9-JS schemes are shown in Table 2. Similar to the previous example, we can see that the new MWENO schemes could keep the designed order of accuracy, while the WENO7-JS scheme could not attain its seventh-order accuracy and the WENO9-JS scheme could keep the ninth-order accuracy in smooth regions. And the absolute truncation errors of two MWENO schemes are smaller than that of the associated same-order WENO schemes once again. Figure 3 shows that the MWENO schemes need less CPU time than the WENO-JS schemes to obtain the same quantities of L^1 and

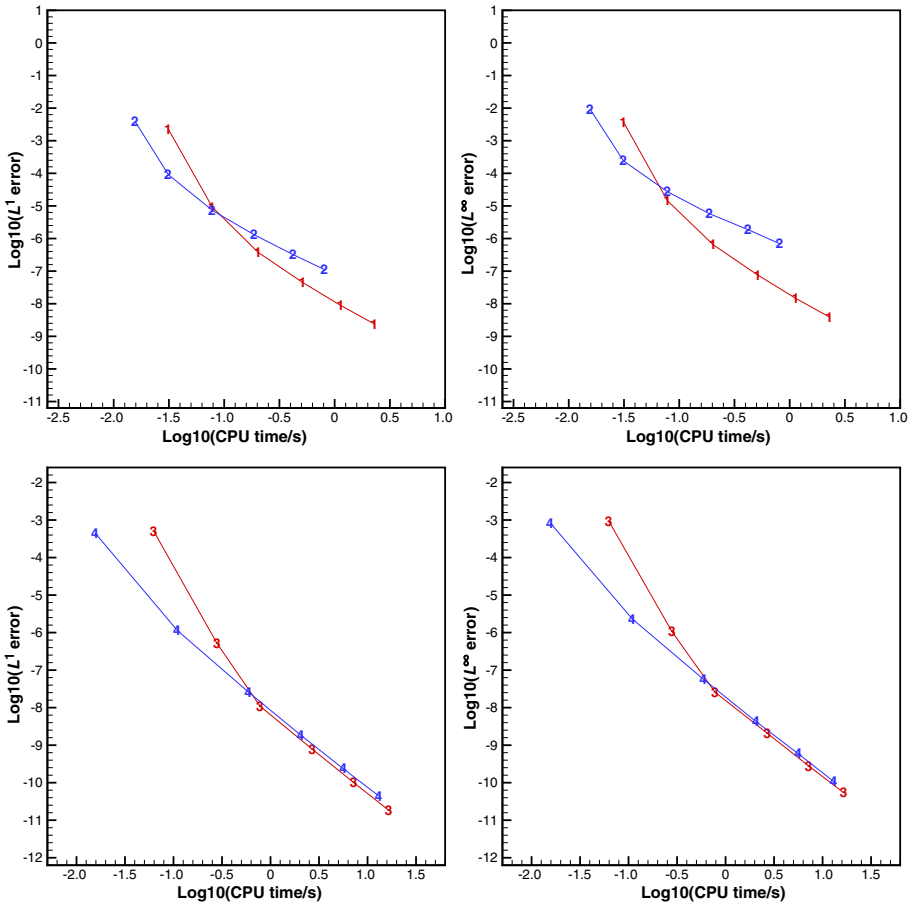

Fig. 2 $u_t + u_x = 0$, $u(x,0) = \sin(\pi x)$. Computing time and error. Number signs "1" and a solid line denote the results of seventh-order MWENO scheme; number signs "2" and a solid line denote the results of seventh-order WENO-JS scheme; number signs "3" and a solid line denote the results of ninth-order MWENO scheme; number signs "4" and a solid line denote the results of ninth-order WENO-JS scheme

L^∞ errors, so the MWENO schemes are more efficient than the WENO-JS schemes in this one-dimensional example.

Example 3 We solve the linear equation in two dimensions:

$$u_t + u_x + u_y = 0, \quad (x,y) \in [0,2] \times [0,2], \tag{59}$$

Table 2 1D-Euler equations: initial data $\rho(x,0) = 1 + 0.2\sin(\pi x)$, $u(x,0) = 1.0$, and $p(x,0) = 1$. $T = 2$. L^1 and L^∞ errors

Grid points	MWENO7 scheme				WENO7-JS scheme			
	L^1 error	Order	L^∞ error	Order	L^1 error	Order	L^∞ error	Order
10	3.13E–4		6.17E–4		8.40E–4		1.45E–3	
20	8.13E–7	8.59	1.35E–6	8.84	1.07E–5	6.29	2.55E–5	5.82
30	2.48E–8	8.60	4.52E–8	8.37	7.84E–7	6.46	2.58E–6	5.65
40	2.44E–9	8.06	4.57E–9	7.96	1.34E–7	6.12	4.96E–7	5.74
50	4.46E–10	7.62	8.15E–10	7.73	3.02E–8	6.70	1.55E–7	5.21
60	1.15E–10	7.42	2.06E–10	7.54	8.89E–9	6.71	5.09E–8	6.10
Grid points	MWENO9 scheme				WENO9-JS scheme			
	L^1 error	Order	L^∞ error	Order	L^1 error	Order	L^∞ error	Order
10	1.78E–4		2.92E–4		1.03E–4		2.24E–4	
20	2.03E–7	9.77	4.06E–7	9.49	4.52E–7	7.84	8.08E–7	8.12
30	4.61E–9	9.34	1.04E–8	9.03	1.10E–8	9.16	2.33E–8	8.74
40	3.34E–10	9.12	7.38E–10	9.21	7.82E–10	9.20	1.74E–9	9.03
50	4.42E–11	9.07	1.03E–10	8.82	1.02E–10	9.11	2.26E–10	9.14
60	8.74E–12	8.89	2.10E–11	8.72	1.92E–11	9.16	4.69E–11	8.64

with the initial condition $u(x,y,0) = \sin(\pi(x+y))$ and the periodic boundary conditions are applied in both directions. The final time is $t = 2$. The errors and numerical orders of accuracy for the MWENO7 scheme, MWENO9 scheme, WENO7-JS scheme, and WENO9-JS scheme are shown in Table 3. Similar to the one-dimensional test cases, we find that the new MWENO schemes would keep the designed order of accuracy; simultaneously, the WENO7-JS scheme could not keep its seventh-order accuracy and the WENO9-JS scheme could keep its ninth-order accuracy again. And the absolute truncation errors of MWENO schemes are smaller than that of the same-order accurate WENO schemes. Figure 4 shows that the MWENO schemes need less CPU time than the WENO-JS schemes to obtain the same quantities of L^1 and L^∞ errors, so the MWENO schemes are more efficient than the WENO-JS schemes in this two-dimensional scalar example.

Example 4 We solve the two-dimensional Euler equations:

$$\frac{\partial}{\partial t}\begin{pmatrix}\rho\\ \rho u\\ \rho v\\ E\end{pmatrix} + \frac{\partial}{\partial x}\begin{pmatrix}\rho u\\ \rho u^2 + p\\ \rho uv\\ u(E+p)\end{pmatrix} + \frac{\partial}{\partial y}\begin{pmatrix}\rho v\\ \rho uv\\ \rho v^2 + p\\ v(E+p)\end{pmatrix} = 0. \tag{60}$$

The initial conditions are $\rho(x,y,0) = 1 + 0.2\sin(\pi(x+y))$, $u(x,y,0) = 0.7$, $v(x,y,0) = 0.3$, and $p(x,y,0) = 1$. The computational domain is $(x,y) \in [0,2] \times [0,2]$. Periodic boundary conditions are applied in both directions. The exact density solution is $\rho(x,y,t) = 1 + 0.2\sin(\pi(x+y-t))$. The final time is $t = 2$. The errors and numerical orders of accuracy for the MWENO7 and MWENO9 schemes together with two classical WENO

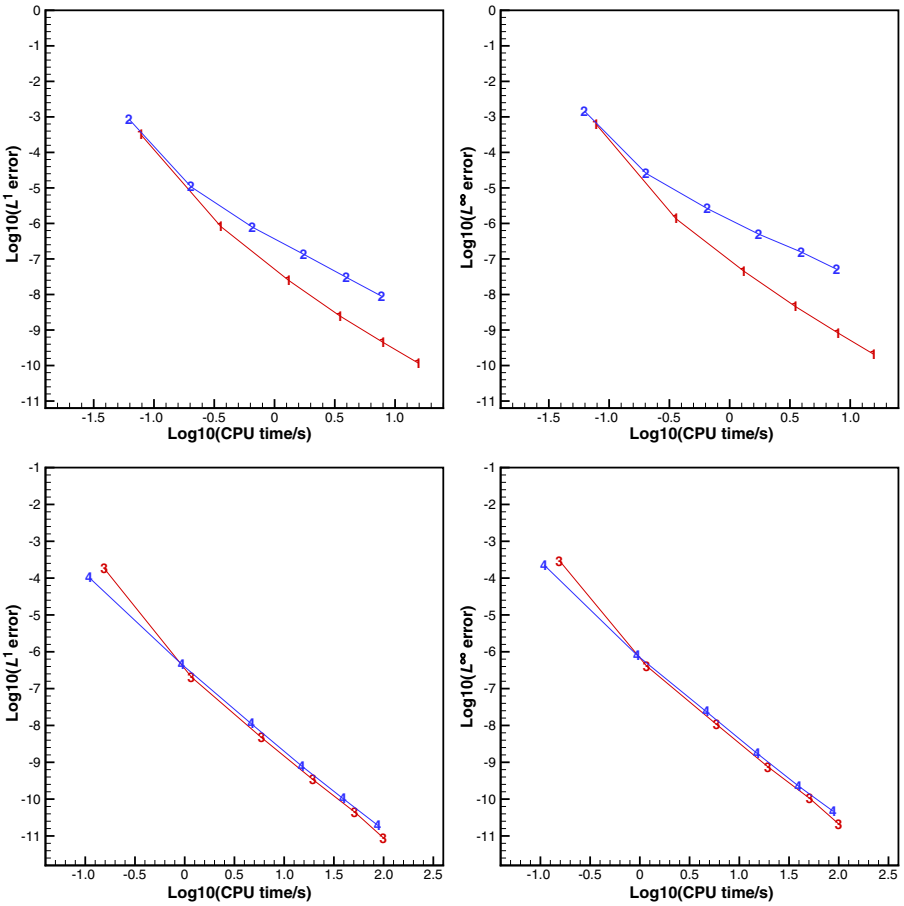

Fig. 3 1D-Euler equations. Computing time and error. Number signs "1" and a solid line denote the results of seventh-order MWENO scheme; number signs "2" and a solid line denote the results of seventh-order WENO-JS scheme; number signs "3" and a solid line denote the results of ninth-order MWENO scheme; number signs "4" and a solid line denote the results of ninth-order WENO-JS scheme

schemes are shown in Table 4. The proposed MWENO schemes with unequal-sized stencils could keep the designed order of accuracy and the WENO7-JS scheme degrades its numerical accuracy again. The associated absolute truncation errors in L^1 and L^∞ norms show that the new high-order MWENO schemes could get more convincing results for this example. Figure 5 shows that the MWENO schemes need less CPU time than the WENO-JS schemes to obtain the same quantities of L^1 and L^∞ errors, so the MWENO schemes are more efficient than the WENO-JS schemes in this two-dimensional example.

Example 5 We consider the one-dimensional Euler equations (58) with a Riemann initial condition for the Lax problem [27]: $(\rho, u, p)^{\mathrm{T}} = (0.445, 0.698, 3.528)^{\mathrm{T}}$ for $x \in [-5, 0)$; $(\rho, u, p)^{\mathrm{T}} = (0.5, 0, 0.571)^{\mathrm{T}}$ for $x \in [0, 5]$. The computed density ρ is plotted at t=1.3 against

Table 3 $u_t + u_x + u_y = 0$, $u(x, y, 0) = \sin(\pi(x + y))$. $T = 2$. L^1 and L^∞ errors

Grid points	MWENO7 scheme				WENO7-JS scheme			
	L^1 error	Order	L^∞ error	Order	L^1 error	Order	L^∞ error	Order
10× 10	4.45E–3		6.87E–3		7.84E–3		1.56E–2	
20× 20	1.99E–5	7.80	2.94E–5	7.86	1.88E–4	5.38	4.26E–4	5.20
30× 30	8.58E–7	7.76	1.38E–6	7.54	1.40E–5	6.39	4.87E–5	5.35
40× 40	1.02E–7	7.38	1.65E–7	7.38	2.57E–6	5.91	1.04E–5	5.35
50× 50	2.03E–8	7.24	3.24E–8	7.31	6.30E–7	6.31	3.32E–6	5.14
60× 60	5.52E–9	7.16	8.79E–9	7.16	2.16E–7	5.86	1.24E–6	5.37
Grid points	MWENO9 scheme				WENO9-JS scheme			
	L^1 error	Order	L^∞ error	Order	L^1 error	Order	L^∞ error	Order
10× 10	9.79E–4		1.73E–3		5.71E–4		1.26E–3	
20× 20	1.09E–6	9.80	2.11E–6	9.68	2.46E–6	7.86	4.59E–6	8.10
30× 30	2.37E–8	9.45	5.45E–8	9.02	5.53E–8	9.36	1.22E–7	8.93
40× 40	1.71E–9	9.13	4.04E–9	9.04	3.96E–9	9.16	8.55E–9	9.26
50× 50	2.22E–10	9.16	5.67E–10	8.80	5.08E–10	9.21	1.22E–9	8.72
60× 60	4.16E–11	9.18	1.09E–10	9.02	9.59E–11	9.14	2.33E–10	9.06

the exact solution in Fig. 6. The MWENO7 and MWENO9 schemes could get similar results and show less oscillations in the region of [2, 3.2].

Example 6 A higher order scheme would show its advantage when the solution contains both shocks and complex smooth region structures. A typical example for this is the shock interaction with entropy wave problem [46]. We solve the one-dimensional Euler equations (58) with a moving Ma=3 shock interacting with sine waves in density: $(\rho, u, p)^{\mathrm{T}} = (3.857\,143, 2.629\,369, 10.333\,333)^{\mathrm{T}}$ for $x \in [-5, -4)$; $(\rho, u, p)^{\mathrm{T}} = (1 + 0.2\sin(5x), 0, 1)^{\mathrm{T}}$ for $x \in [-4, 5]$. The computed density ρ is plotted at t=1.8 against the referenced "exact" solution which is a converged solution computed by the fifth-order finite difference WENO-JS scheme [24] with 2 000 grid points in Fig. 7. The MWENO7 and MWENO9 schemes could get better resolution in the region of $[-0.8, 2.4]$ with only 100 points in the computational field.

Example 7 We compute the interaction of the blast wave problem [50] by solving the Euler equations (58) with the initial conditions: $(\rho, u, p)^{\mathrm{T}} = (1, 0, 1\,000)^{\mathrm{T}}$ for $x \in [0, 0.1)$; $(\rho, u, p)^{\mathrm{T}} = (1, 0, 0.01)^{\mathrm{T}}$ for $x \in [0.1, 0.9)$; $(\rho, u, p)^{\mathrm{T}} = (1, 0, 100)^{\mathrm{T}}$ for $x \in [0.9, 1.0]$. The computed density ρ is plotted at t=0.038 against the referenced "exact" solution which is a converged solution computed by the fifth-order finite difference WENO scheme [24] with 2 000 grid points in Fig. 8. The MWENO7 and MWENO9 schemes could get sharp sock transitions in the computational fields. And the WENO7-JS and WENO9-JS schemes could not do associated computations for the sake of their usage of the information in more wider stencils to reconstruct high-degree polynomials than that of the MWENO schemes. Therefore, it results in the collapse of the programs of the WENO7-JS and WENO9-JS schemes.

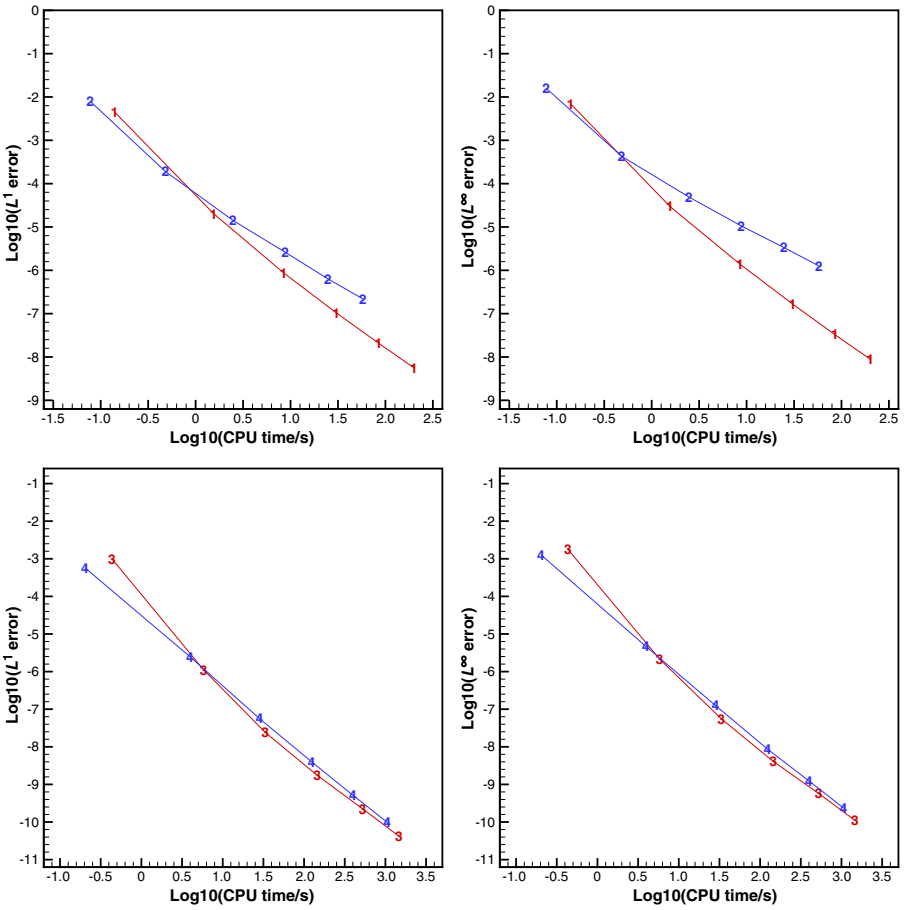

Fig. 4 $u_t + u_x + u_y = 0$, $u(x, y, 0) = \sin(\pi(x + y))$. Computing time and error. Number signs "1" and a solid line denote the results of seventh-order MWENO scheme; number signs "2" and a solid line denote the results of seventh-order WENO-JS scheme; number signs "3" and a solid line denote the results of ninth-order MWENO scheme; number signs "4" and a solid line denote the results of ninth-order WENO-JS scheme

Example 8 The one-dimensional Sedov blast wave problem [26, 37]. This problem contains very low density with strong shocks. The exact solution is specified in [26, 37]. The computing domain is $[-2, 2]$ and the initial conditions are $\rho = 1$, $u = 0$, $E = 10^{-12}$ everywhere except that the energy in the center point is the constant $\frac{3\,200\,000}{\Delta x}$. The inlet and outlet conditions are imposed on the left and right boundaries, respectively. The final computing time is $T = 0.001$. The computational results by the seventh-order and ninth-order

Table 4 2D-Euler equations: initial data $\rho(x, y, 0) = 1 + 0.2\sin(\pi(x + y))$, $u(x, y, 0) = 0.7$, $v(x, y, 0) = 0.3$, and $p(x, y, 0) = 1$. $T = 2$. L^1 and L^∞ errors

Grid points	MWENO7 scheme				WENO7-JS scheme			
	L^1 error	Order	L^∞ error	Order	L^1 error	Order	L^∞ error	Order
10× 10	5.60E–4		8.31E–4		9.53E–4		2.23E–3	
20× 20	2.38E–6	7.88	3.79E–6	7.78	2.49E–5	5.26	6.34E–5	5.14
30× 30	1.01E–7	7.78	1.70E–7	7.66	1.95E–6	6.28	6.97E–6	5.45
40× 40	1.19E–8	7.43	2.01E–8	7.42	3.43E–7	6.04	1.51E–6	5.30
50× 50	2.35E–9	7.27	3.89E–9	7.36	8.33E–8	6.35	4.45E–7	5.50
60× 60	6.36E–10	7.19	1.05E–9	7.18	2.59E–8	6.39	1.57E–7	5.70
Grid points	MWENO9 scheme				WENO9-JS scheme			
	L^1 error	Order	L^∞ error	Order	L^1 error	Order	L^∞ error	Order
10× 10	1.22E–4		2.13E–4		8.80E–5		1.86E–4	
20× 20	1.28E–7	9.90	2.74E–7	9.60	3.26E–7	8.07	6.12E–7	8.25
30× 30	2.81E–9	9.42	6.83E–9	9.11	7.62E–9	9.27	1.66E–8	8.89
40× 40	2.03E–10	9.14	4.98E–10	9.10	5.31E–10	9.26	1.16E–9	9.24
50× 50	2.69E–11	9.06	6.71E–11	8.98	6.77E–11	9.23	1.59E–10	8.92
60× 60	5.09E–12	9.12	1.26E–11	9.16	1.24E–11	9.28	3.22E–11	8.77

MWENO schemes including the density, velocity, and pressure are shown in Fig. 9. We can see that the MWENO schemes work well for this extreme example.

Example 9 The one-dimensional double rarefaction wave problem [32]. This test case has the low pressure and low-density regions and is hard to be simulated precisely. The initial conditions are $(\rho, u, p, \gamma)^{\mathrm{T}} = (7, -1, 0.2, 1.4)^{\mathrm{T}}$ for $x \in [-1, 0)$; $(\rho, u, p, \gamma)^{\mathrm{T}} = (7, 1, 0.2, 1.4)^{\mathrm{T}}$ for $x \in [0, 1]$. The inlet and outlet conditions are imposed on the left and right boundaries, respectively. The final computing time is $T = 0.6$. The computational results computed by the seventh-order and ninth-order MWENO schemes including the density, velocity, and pressure are shown in Fig. 10. It is obvious that the MWENO7 and MWENO9 schemes could get good performance for this extreme one-dimensional example.

Example 10 The Leblanc problem [32]. The initial conditions are $(\rho, u, p, \gamma)^{\mathrm{T}} = (2, 0, 10^9, 1.4)^{\mathrm{T}}$ for $x \in [-10, 0)$; $(\rho, u, p, \gamma)^{\mathrm{T}} = (0.001, 0, 1, 1.4)^{\mathrm{T}}$ for $x \in [0, 10]$. The final computing time is $t = 0.000\,1$. The computational results of the density are shown in Fig. 11. We could get reasonable results by the usage of the MWENO7 and MWENO9 schemes. And once again, the WENO7-JS and WENO9-JS schemes could not do associated computations.

Example 11 Double Mach reflection problem. This model problem is originally from [50]. We solve the two-dimensional Euler equations (60) in a computational domain of $[0, 4] \times [0, 1]$. The reflection boundary condition is used at the wall, which for the rest

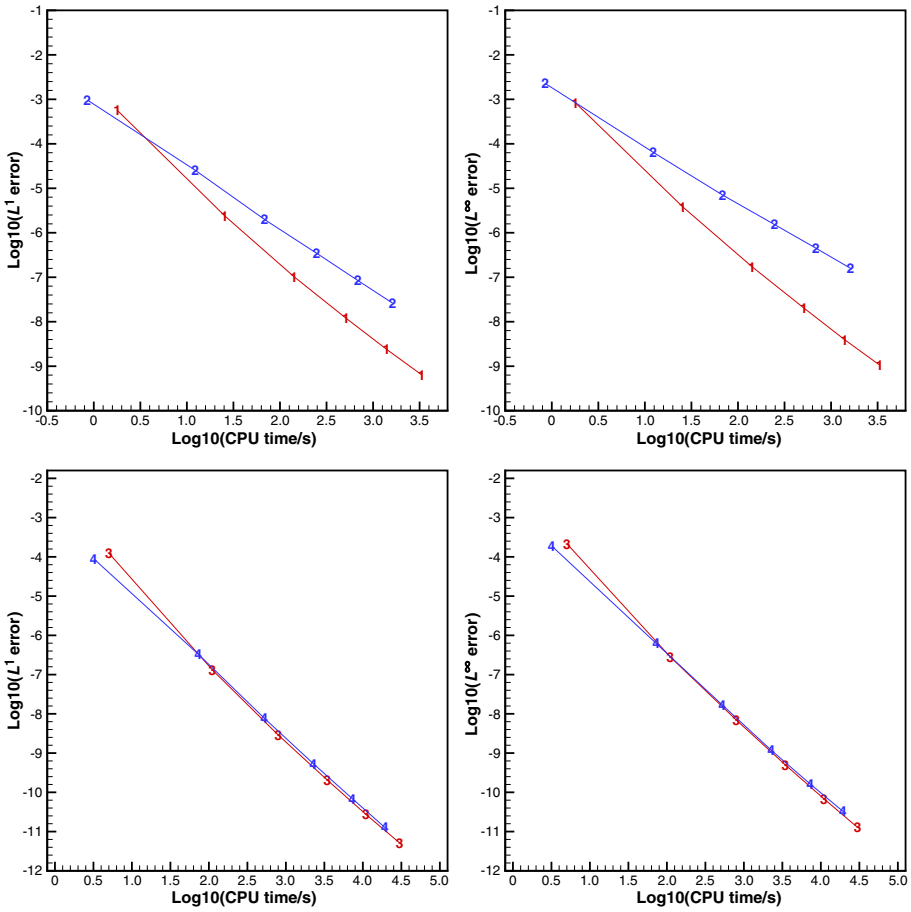

Fig. 5 2D-Euler equations. Computing time and error. Number signs "1" and a solid line denote the results of seventh-order MWENO scheme; number signs "2" and a solid line denote the results of seventh-order WENO-JS scheme; number signs "3" and a solid line denote the results of ninth-order MWENO scheme; number signs "4" and a solid line denote the results of ninth-order WENO-JS scheme

of the bottom boundary (the part from $x = 0$ to $x = \frac{1}{6}$), the exact post-shock condition is imposed. There is an exact motion of the Ma=10 shock at the top boundary. The results are shown at t=0.2. The seventh-order and ninth-order MWENO schemes are applied in this example and the simulation results are shown in Fig. 12. Clearly, the resolution computed by the MWENO7 and MWENO9 schemes could give good resolution with an increasing numerical order on grid points $1\,600 \times 400$.

Example 12 Forward step problem. This model problem is also originally from [50]. The setup of the problem is as follows. The wind tunnel is 1 length unit wide and 3 length units long. The step is 0.2 length units high and is located 0.6 length units from the left-hand end of the tunnel. The problem is initialized by a right-going Ma=3 flow. Reflective boundary

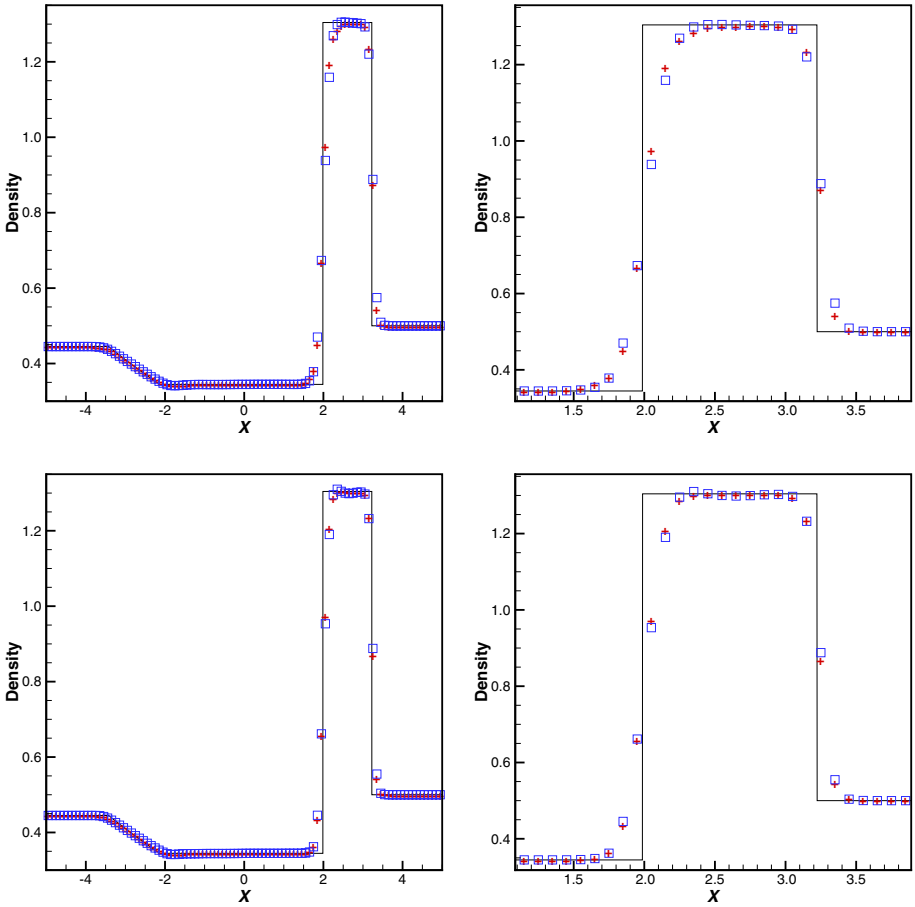

Fig. 6 The Lax problem. T=1.3. From left to right: density; density zoomed in. From top to bottom: seventh-order scheme; ninth-order scheme. Solid line: the exact solution; plus signs: the results of MWENO schemes; squares: the results of WENO-JS schemes. Grid points: 100

conditions are applied along the wall of the tunnel and inflow/outflow boundary conditions are applied at the entrance/exit. The results are shown at $t = 4$. In Fig. 13, we show 30 equally spaced density contours from 0.32 to 6.15 computed by the MWENO7 scheme and MWENO9 scheme. We can clearly observe that the different high-order schemes work well especially for the resolution of the physical instability and roll-up of the contact line on grid points 600×200.

Example 13 The two-dimensional Sedov blast wave problem [26, 37]. The initial conditions are ρ=1, u=0, v=0, E=10^{-12} everywhere except that the energy in the lower left corner point is the constant $\frac{0.244\,816}{\Delta x \Delta y}$, and $\gamma = 1.4$. The reflective conditions are imposed on the left and bottom boundaries, and the outlet conditions are imposed on the right and top boundaries, respectively. The final time is $T = 1$. The numerical results computed by the

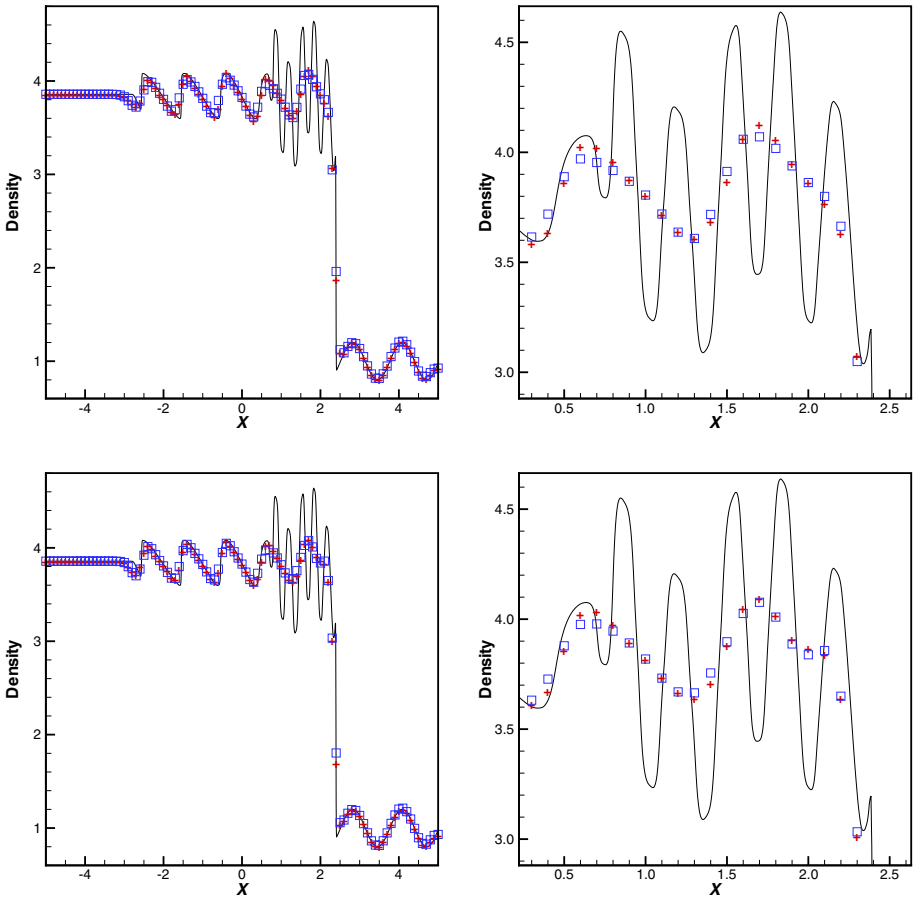

Fig. 7 The shock density wave interaction problem. T=1.8. From left to right: density; density zoomed in. From top to bottom: seventh-order scheme; ninth-order scheme. Solid line: the referenced "exact" solution; plus signs: the results of MWENO schemes; squares: the results of WENO-JS schemes. Grid points: 100

seventh-order and ninth-order MWENO schemes are shown in Fig. 14. Again, it is observed that high-order MWENO schemes work well for this extreme example.

Example 14 The two-dimensional double rarefaction wave problem [32]. The initial conditions are $(\rho, u, v, p, \gamma)^{\mathrm{T}} = (7, -1, 0, 0.2, 1.4)^{\mathrm{T}}$ for $(x, y) \in [-1, 0) \times [-1, 1]$; $(\rho, u, v, p, \gamma)^{\mathrm{T}} = (7, 1, 0, 0.2, 1.4)^{\mathrm{T}}$ for $(x, y) \in [0, 1] \times [-1, 1]$. The inflow boundary condition is used on the left boundary and outflow boundary condition is used on the other three boundaries. The final computing time is $T = 0.6$. The numerical results computed by the high-order MWENO schemes including the density, velocity, and pressure are shown in Fig. 15. We can see that these MWENO schemes work well for this extreme example once again.

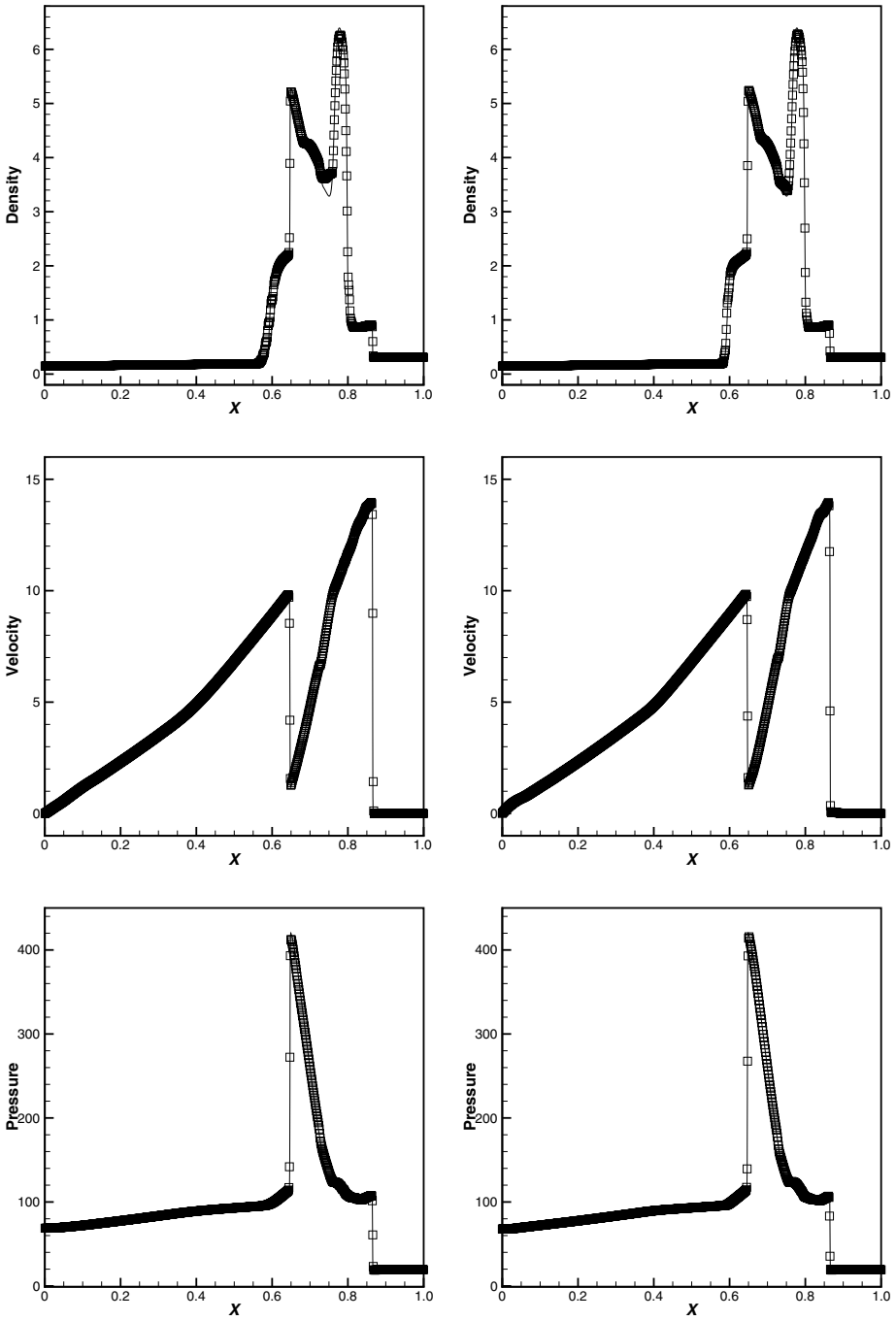

Fig. 8 The blast wave problem. Solid line: the referenced "exact" solution; squares: the results of MWENO schemes. From left to right: seventh-order scheme; ninth-order scheme. From top to bottom: density, velocity, and pressure. Grid points: 800

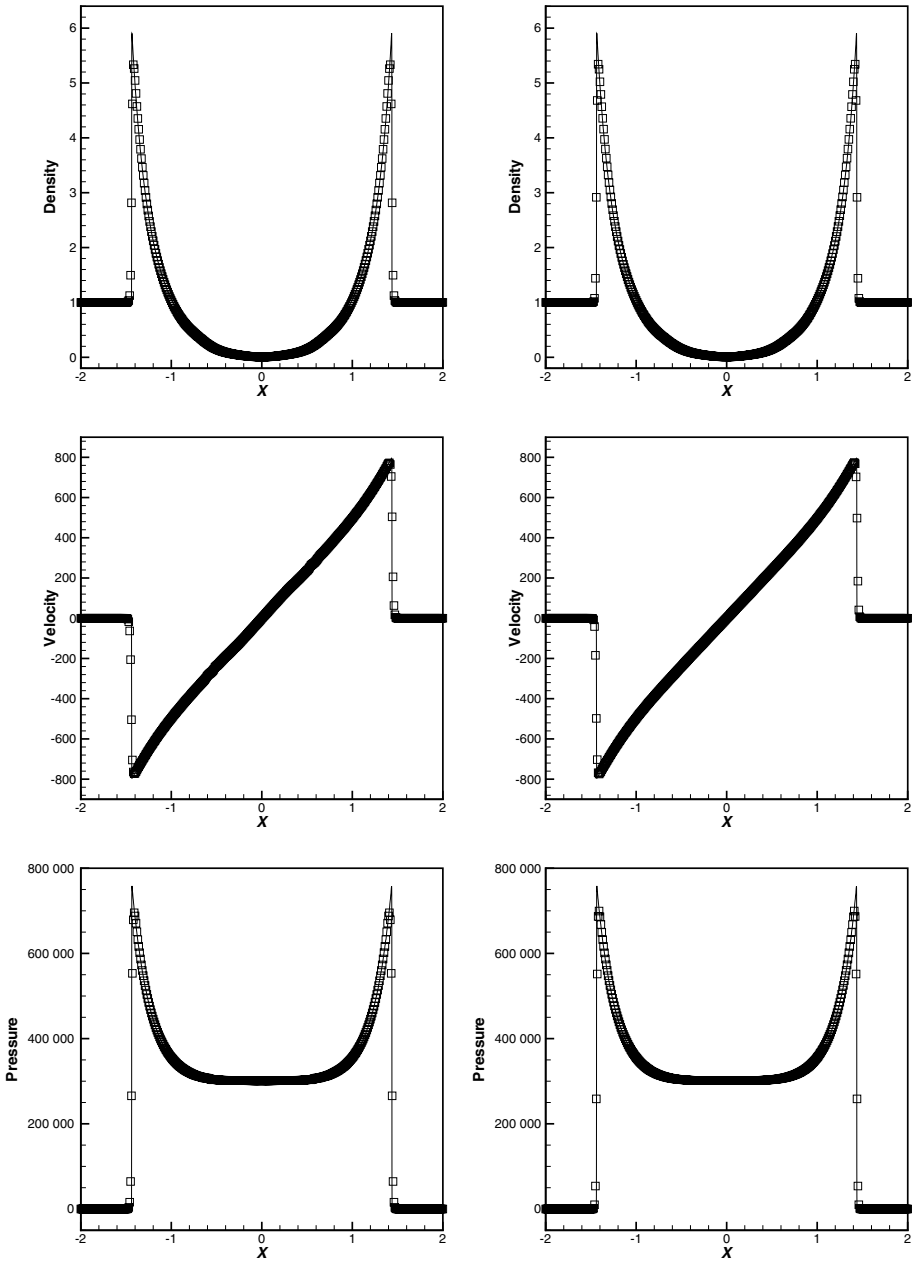

Fig. 9 The Sedov blast wave problem. T=0.001. Solid line: the exact solution; squares: the results of MWENO schemes. From left to right: seventh-order scheme; ninth-order scheme. From top to bottom: density, velocity, and pressure. Grid points: 400

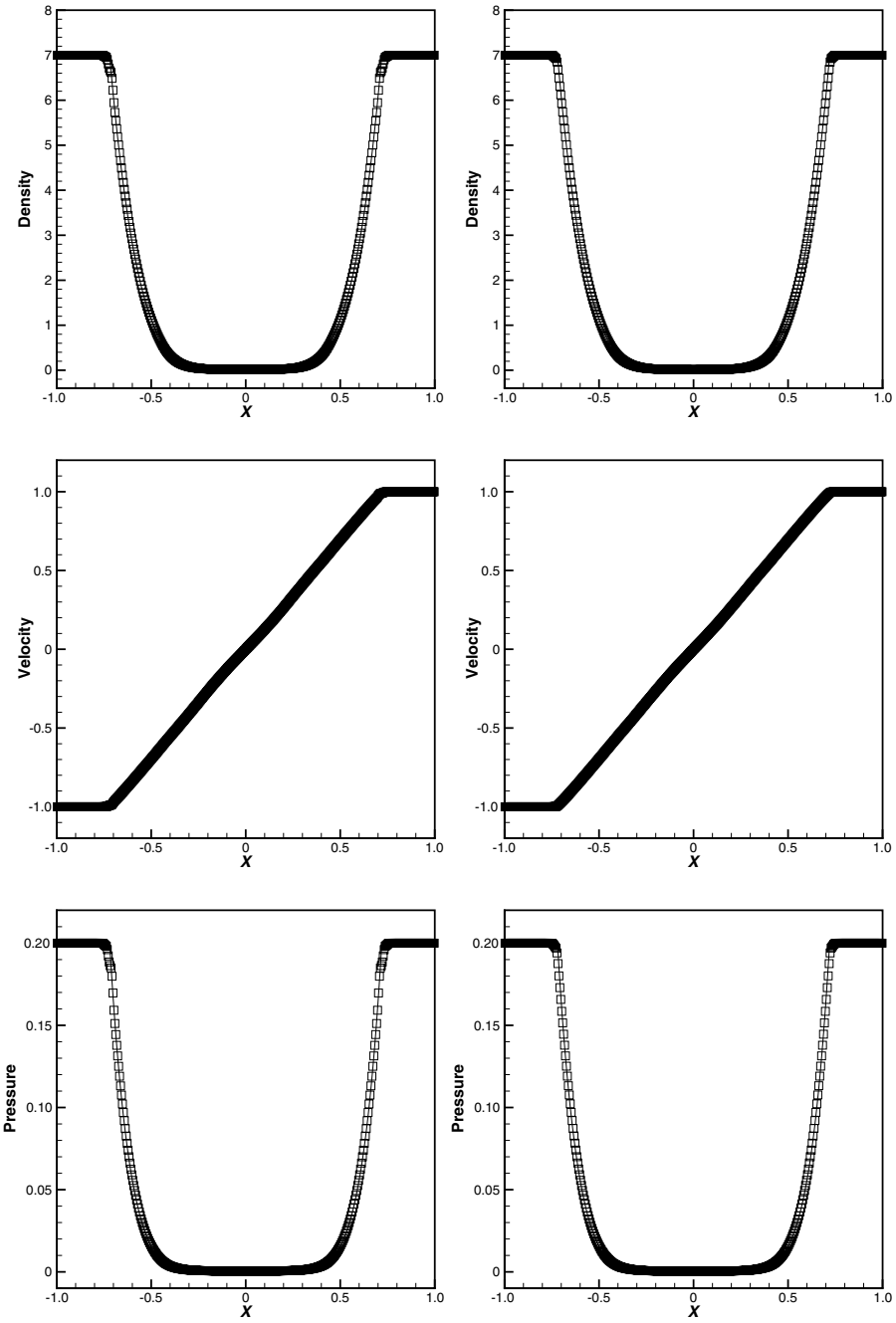

Fig. 10 The double rarefaction wave problem. T=0.6. Solid line: the exact solution; squares: the results of MWENO schemes. From left to right: seventh-order scheme; ninth-order scheme. From top to bottom: density, velocity, and pressure. Grid points: 400

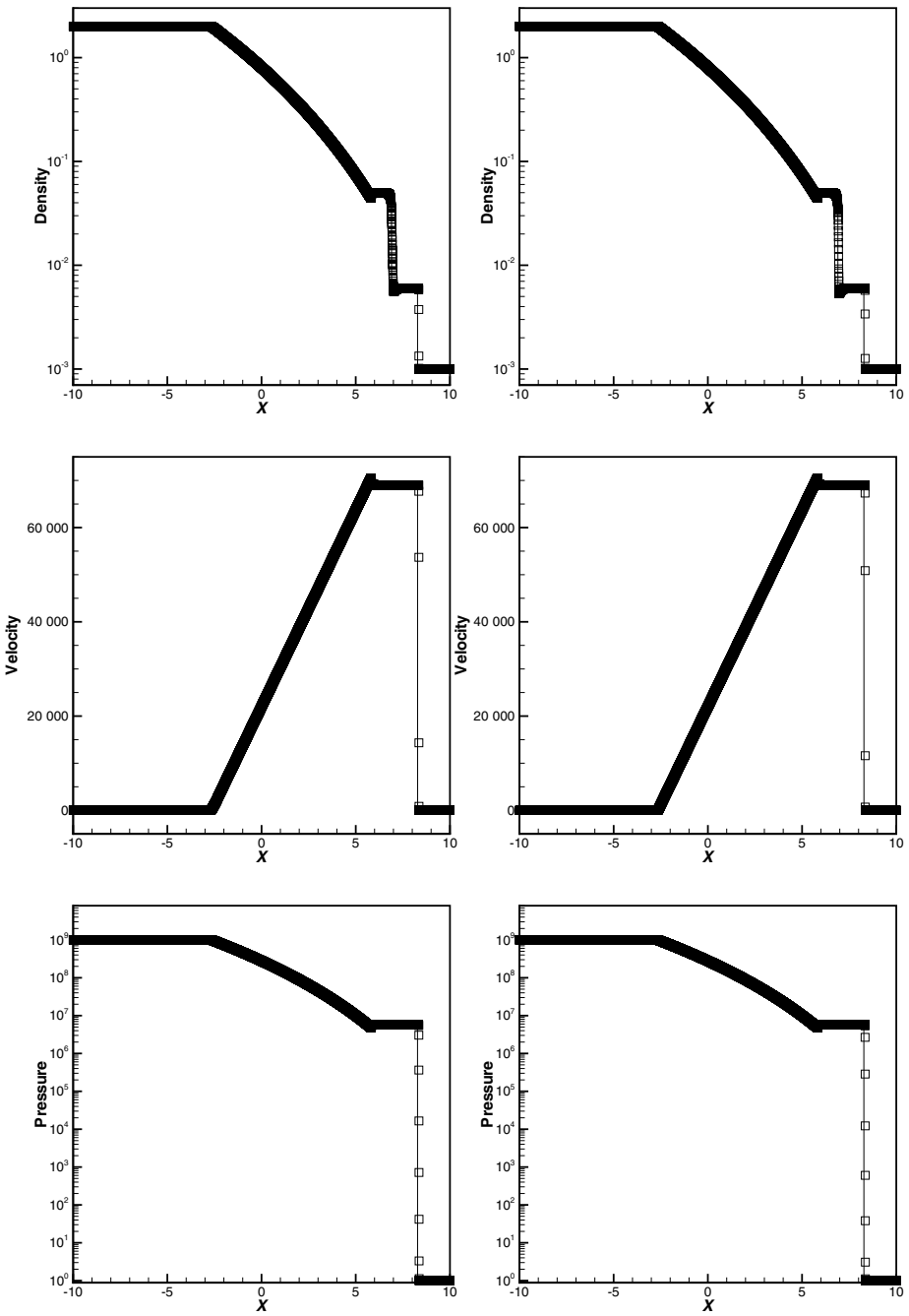

Fig. 11 The Leblanc problem. T=0.000 1. Solid line: the exact solution; squares: the results of MWENO schemes. From left to right: seventh-order scheme; ninth-order scheme. From top to bottom: log plot of density, velocity, and log plot of pressure. Grid points: 6 400

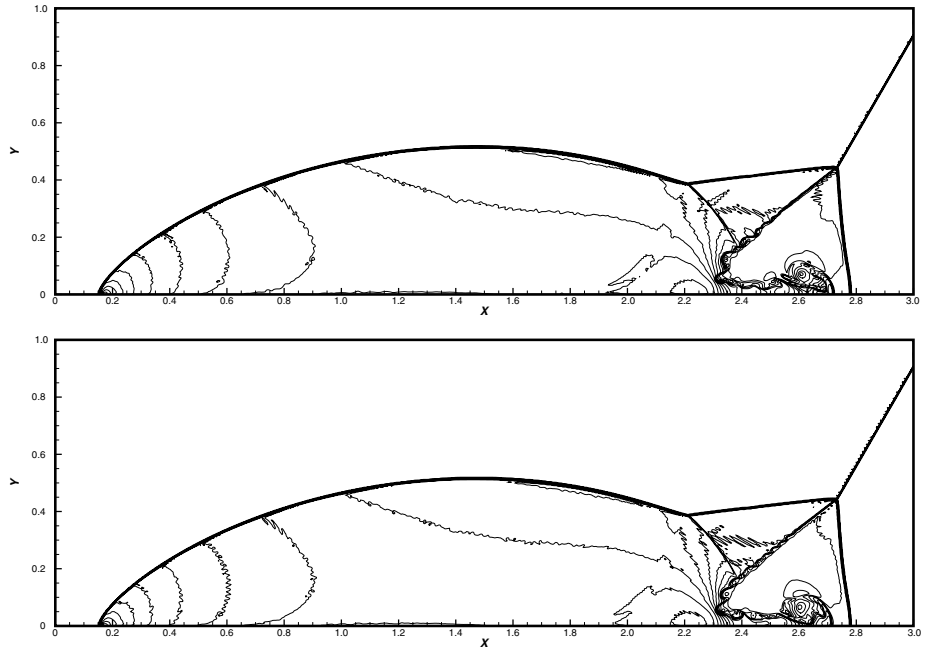

Fig. 12 Double Mach reflection problem. T=0.2. Thirty equally spaced density contours from 1.5 to 22.7. Top: MWENO7 scheme; bottom: MWENO9 scheme. Grid points: $1\,600 \times 400$

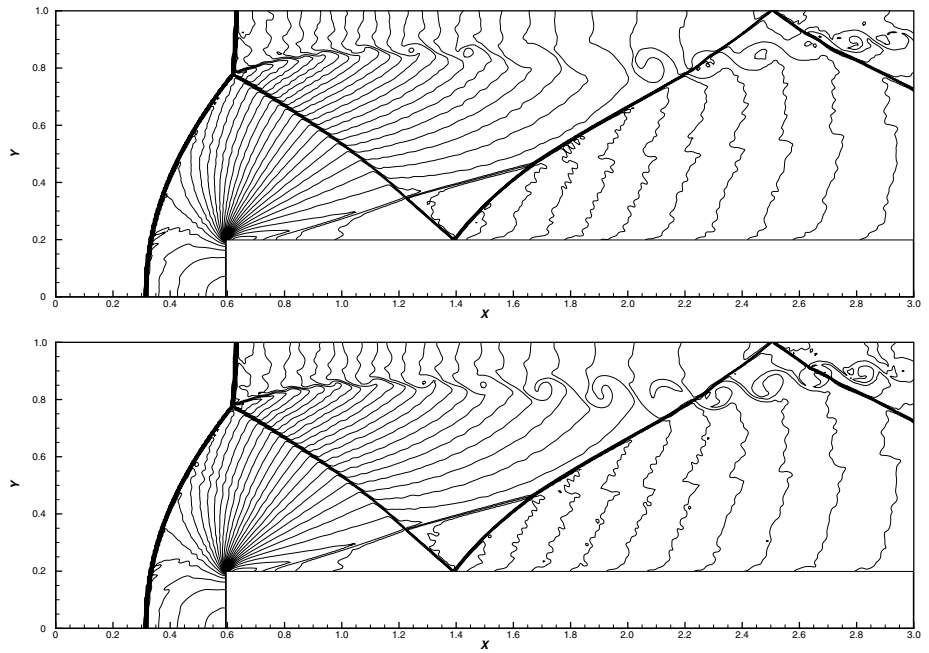

Fig. 13 Forward step problem. T=4. Thirty equally spaced density contours from 0.32 to 6.15. From top to bottom: MWENO7 scheme; MWENO9 scheme. Grid points: 600×200

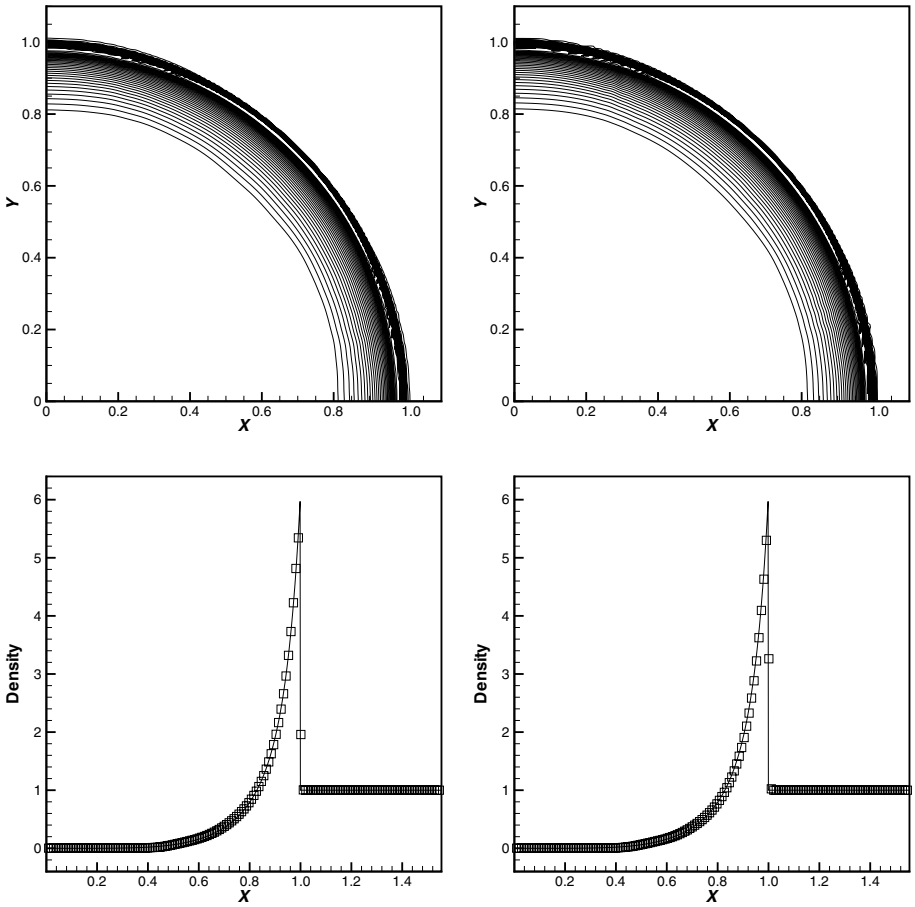

Fig. 14 The 2D Sedov problem. T=1. From top to bottom: 30 equally spaced density contours from 0.95 to 5; density is projected to the radical coordinates. Solid line: the exact solution; squares: the results of MWENO schemes. From left to right: seventh-order scheme; ninth-order scheme. Grid points: 160×160

4 Concluding Remarks

In this paper, we design the new seventh-order and ninth-order finite difference MWENO schemes equipped with a series of unequal-sized stencils for solving hyperbolic conservation laws on structured meshes. One crucial innovation of the new high-order finite difference MWENO schemes is to introduce a splitting stencil methodology to obtain a series of unequal-sized stencils and reconstruct different degree polynomials defined on them. Thereafter, we compute the linear weights and the smoothness indicators as specified in [24], and propose a series of new mapping functions to obtain the mapped nonlinear weights for the purpose of decreasing the difference quantity between the mapped nonlinear weights and the linear weights. Together with the application of the third-order Runge-Kutta time discretization method [45], we can design high-order finite difference MWENO schemes with a normal CFL number and without introducing any monotonicity preserving procedures [3] to obtain optimal high-order accuracy in

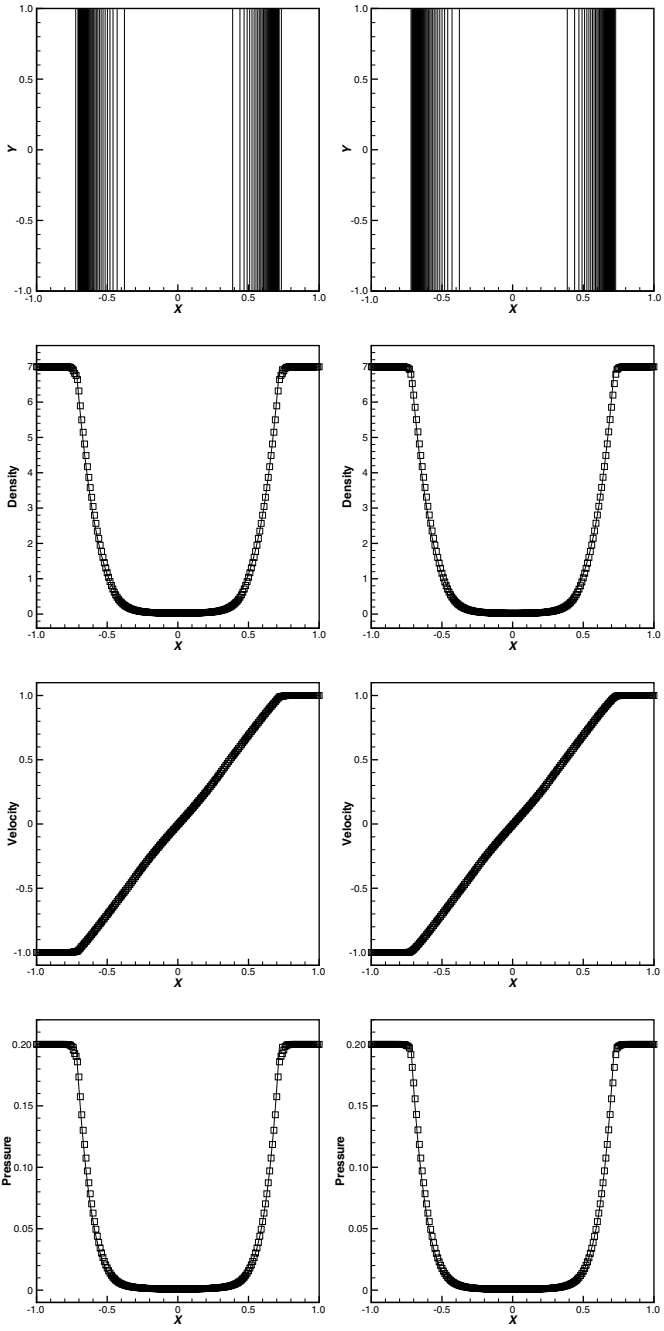

Fig. 15 The 2D double rarefaction wave problem. T=0.6. From top to bottom: 30 equally spaced density contours from 0.25 to 6.77; cut at $y = 0$ for the 2D problem: density, velocity, and pressure. Solid line: the exact solution; squares: the results of MWENO schemes. From left to right: seventh-order scheme; ninth-order scheme. Grid points: 200×200

smooth regions and keep essentially non-oscillatory property in non-smooth regions. We emphasize a fact that the use of the mapping functions in [4, 5, 9, 12, 14, 20, 21] is to improve the accuracy at smooth extrema, but the use of our new mapping functions is to decrease the difference quantity between the new mapped nonlinear weights and the linear weights. In comparison to the classical high-order WENO schemes [3, 44] with equal-sized stencils, the new MWENO schemes with unequal-sized stencils are very robust in the computation of some benchmark extreme examples containing the strong shocks, contact discontinuities, and rarefaction waves.

Compliance with Ethical Standards

Conflict of Interest On behalf of all authors, the corresponding author states that there is no conflict of interest.

References

1. Balsara, D.S., Garain, S., Shu, C.-W.: An efficient class of WENO schemes with adaptive order. J. Comput. Phys. **326**, 780–804 (2016)
2. Balsara, D.S., Rumpf, T., Dumbser, M., Munz, C.D.: Efficient, high accuracy ADER-WENO schemes for hydrodynamics and divergence-free magnetohydrodynamics. J. Comput. Phys. **228**, 2480–2516 (2009)
3. Balsara, D.S., Shu, C.-W.: Monotonicity preserving weighted essentially non-oscillatory schemes with increasingly high order of accuracy. J. Comput. Phys. **160**, 405–452 (2000)
4. Borges, R., Carmona, M., Costa, B., Don, W.S.: An improved weighted essentially non-oscillatory scheme for hyperbolic conservation laws. J. Comput. Phys. **227**, 3191–3211 (2008)
5. Bryson, S., Levy, D.: Mapped WENO and weighted power ENO reconstructions in semi-discrete central schemes for Hamilton-Jacobi equations. Appl. Numer. Math. **56**, 1211–1224 (2006)
6. Capdeville, G.: A central WENO scheme for solving hyperbolic conservation laws on non-uniform meshes. J. Comput. Phys. **227**, 2977–3014 (2008)
7. Casper, J.: Finite-volume implementation of high order essentially nonoscillatory schemes in two dimensions. AIAA J. **30**, 2829–2835 (1992)
8. Casper, J., Atkins, H.L.: A finite-volume high order ENO scheme for two-dimensional hyperbolic systems. J. Comput. Phys. **106**, 62–76 (1993)
9. Castro, M., Costa, B., Don, W.S.: High order weighted essentially non-oscillatory WENO-Z schemes for hyperbolic conservation laws. J. Comput. Phys. **230**, 1766–1792 (2011)
10. Colella, P., Woodward, P.: The piecewise parabolic method (PPM) for gas-dynamical simulations. J. Comput. Phys. **54**, 174–201 (1984)
11. Cravero, I., Semplice, M.: On the accuracy of WENO and CWENO reconstructions of third order on nonuniform meshes. J. Sci. Comput. **67**, 1219–1246 (2016)
12. Feng, H., Hu, F.X., Wang, R.: A new mapped weighted essentially non-oscillatory scheme. J. Sci. Comput. **51**, 449–473 (2012)
13. Fu, L., Hu, X.Y.Y., Adams, N.A.: A family of high order targeted ENO schemes for compressible-fluid simulations. J. Comput. Phys. **305**, 333–359 (2016)
14. Gao, Z., Don, W.S.: Mapped hybrid central-WENO finite difference scheme for detonation waves simulations. J. Sci. Comput. **55**, 351–371 (2013)
15. Godunov, S.K.: A finite-difference scheme for the numerical computation of discontinuous solutions of the equations of fluid dynamics. Matematicheskii Sbornik **47**(3), 271–290 (1959)
16. Harten, A.: High resolution schemes for hyperbolic conservation laws. J. Comput. Phys. **49**(3), 357–393 (1983)
17. Harten, A.: Preliminary results on the extension of ENO schemes to two-dimensional problems. In: Carasso, C. (ed.) Proceedings, International Conference on Nonlinear Hyperbolic Problems, Saint-Etienne, 1986. Lecture Notes in Mathematics, Springer-Verlag, Berlin (1987)
18. Harten, A., Engquist, B., Osher, S., Chakravarthy, S.: Uniformly high order accurate essentially non-oscillatory schemes III. J. Comput. Phys. **71**, 231–323 (1987)

19. Harten, A., Osher, S.: Uniformly high order accurate non-oscillatory schemes, IMRC Technical Summary Rept. 2823. Univ. of Wisconsin, Madison (1985)
20. Henrick, A.K., Aslam, T.D., Powers, J.M.: Mapped weighted essentially non-oscillatory schemes: achieving optimal order near critical points. J. Comput. Phys. **207**, 542–567 (2005)
21. Hong, Z., Ye, Z., Meng, X.: A mapping-function-free WENO-M scheme with low computational cost. J. Comput. Phys. **405**, 109145 (2020)
22. Hu, G., Li, R., Tang, T.: A robust WENO type finite volume solver for steady Euler equations on unstructured grids. Commun. Comput. Phys. **9**, 627–648 (2011)
23. Hu, C., Shu, C.-W.: Weighted essentially non-oscillatory schemes on triangular meshes. J. Comput. Phys. **150**, 97–127 (1999)
24. Jiang, G.-S., Shu, C.-W.: Efficient implementation of weighted ENO schemes. J. Comput. Phys. **126**, 202–228 (1996)
25. Kolb, O.: On the full and global accuracy of a compact third order WENO scheme. SIAM J. Numer. Anal. **52**(5), 2335–2355 (2014)
26. Korobeinikov, V.P.: Problems of Point-Blast Theory. American Institute of Physics, New York (1991)
27. Lax, P.D.: Weak solutions of nonlinear hyperbolic equations and their numerical computation. Commun. Pure Appl. Math. **7**, 159–193 (1954)
28. Leonard, B.P.: The ULTIMATE conservative difference scheme applied to unsteady one-dimensional advection. Comput. Meth. Appl. Mech. Eng. **88**, 17–74 (1991)
29. Leonard, B.P., Lock, A.P., MacVean, M.K.: The NIRVANA scheme applied to one-dimensional advection. Int. J. Num. Meth. Heat Fluid Flow **5**, 341–377 (1995)
30. Levy, D., Puppo, G., Russo, G.: Central WENO schemes for hyperbolic systems of conservation laws. ESAIM: M2AN **33**, 547–571 (1999)
31. Levy, D., Puppo, G., Russo, G.: Compact central WENO schemes for multidimensional conservation laws. SIAM J. Sci. Comput. **22**(2), 656–672 (2000)
32. Linde, T., Roe, P.L.: Robust Euler codes. In: 13th Computational Fluid Dynamics Conference, AIAA-97-2098, AIAA Inc., Reno, Nevada (1997)
33. Liu, X.D., Osher, S., Chan, T.: Weighted essentially non-oscillatory schemes. J. Comput. Phys. **115**, 200–212 (1994)
34. Liu, Y., Zhang, Y.T.: A robust reconstruction for unstructured WENO schemes. J. Sci. Comput. **54**, 603–621 (2013)
35. Pirozzoli, S.: Conservative hybrid compact-WENO schemes for shock-turbulence interaction. J. Comput. Phys. **178**, 81–117 (2002)
36. Qiu, J., Shu, C.-W.: On the construction, comparison, and local characteristic decomposition for high order central WENO schemes. J. Comput. Phys. **183**, 187–209 (2002)
37. Sedov, L.I.: Similarity and Dimensional Methods in Mechanics. Academic Press, New York (1959)
38. Semplice, M., Coco, A., Russo, G.: Adaptive mesh refinement for hyperbolic systems based on third-order compact WENO reconstruction. J. Sci. Comput. **66**, 692–724 (2016)
39. Serna, S., Marquina, A.: Power-ENO methods: a fifth-order accurate weighted power ENO method. J. Comput. Phys. **194**, 632–658 (2004)
40. Serna, S., Qian, J.: Fifth order weighted power-ENO methods for Hamilton-Jacobi equations. J. Sci. Comput. **29**, 57–81 (2006)
41. Shen, Y.Q., Yang, G.W.: Hybrid finite compact-WENO schemes for shock calculation. Int. J. Numer. Meth. Fluids **53**, 531–560 (2007)
42. Shen, Y.Q., Zha, G.C.: A robust seventh-order WENO scheme and its applications. In: 46th AIAA Aerospace Sciences Meeting and Exhibit, AIAA 2008-757, AIAA, Inc., Reno, Nevada (2008)
43. Shi, J., Hu, C.Q., Shu, C.-W.: A technique of treating negative weights in WENO schemes. J. Comput. Phys. **175**, 108–127 (2002)
44. Shu, C.-W.: Essentially non-oscillatory and weighted essentially non-oscillatory schemes for hyperbolic conservation laws. In: Quarteroni, A. (ed.) Advanced Numerical Approximation of Nonlinear Hyperbolic Equations. Lecture Notes in Mathematics, vol. 1697, pp. 325–432. Springer-Verlag, Berlin, Heidelberg (1998)
45. Shu, C.-W., Osher, S.: Efficient implementation of essentially non-oscillatory shock capturing schemes. J. Comput. Phys. **77**, 439–471 (1988)
46. Shu, C.-W., Osher, S.: Efficient implementation of essentially non-oscillatory shock capturing schemes, II. J. Comput. Phys. **83**, 32–78 (1989)
47. Suresh, A., Huynh, H.T.: Accurate monotonicity preserving scheme with Runge-Kutta time stepping. J. Comput. Phys. **136**, 83–99 (1997)
48. Van Leer, B.: Towards the ultimate conservative difference scheme. V. A second-order sequel to Godunov's method. J. Comput. Phys. **32**, 101–136 (1979)

49. Wang, Z.J., Chen, R.F.: Optimized weighted essentially non-oscillatory schemes for linear waves with discontinuity. J. Comput. Phys. **174**, 381–404 (2001)
50. Woodward, P., Colella, P.: The numerical simulation of two-dimensional fluid flow with strong shocks. J. Comput. Phys. **54**, 115–173 (1984)
51. Zhang, Y.T., Shu, C.-W.: High order WENO schemes for Hamilton-Jacobi equations on triangular meshes. SIAM J. Sci. Comput. **24**, 1005–1030 (2003)
52. Zhang, Y.T., Shu, C.-W.: Third order WENO scheme on three dimensional tetrahedral meshes. Commun. Comput. Phys. **5**, 836–848 (2009)
53. Zhang, X., Shu, C.-W.: On maximum-principle-satisfying high-order schemes for scalar conservation laws. J. Comput. Phys. **229**, 3091–3120 (2010)
54. Zhang, X., Shu, C.-W.: On positivity preserving high order discontinuous Galerkin schemes for compressible Euler equations on rectangular meshes. J. Comput. Phys. **229**, 8918–8934 (2010)
55. Zhang, X., Shu, C.-W.: Maximum-principle-satisfying and positivity-preserving high order schemes for conservation laws: survey and new developments. Proc. R. Soc. A **467**, 2752–2776 (2011)
56. Zhang, X., Shu, C.-W.: Positivity-preserving high order finite difference WENO schemes for compressible Euler equations. J. Comput. Phys. **231**, 2245–2258 (2012)